CERN-PPE/91-223
29 November 1991

EUROPEAN ORGANIZATION FOR NUCLEAR RESEARCH

Lateral Shower Profiles in a Lead/Scintillating-Fiber Calorimeter

D. Acosta[1)], S. Buontempo[2)], L. Calôba[3)], R. DeSalvo[4a)], A. Ereditato[2)], R. Ferrari[5)], G. Fumagalli[5)], G. Goggi[4,5)], W. Hao[6)]†, A. Henriques[4,7)], L. Linssen[4a)], M. Livan[8)], A. Maio[7)], M.R. Mondardini[9)], B. Ong[1)], H.P. Paar[1)], F. Pastore[5)], E. Pennacchio[5)], L. Poggioli[4,10)], G. Polesello[4,5)], F. Riccardi[2)], A. Rimoldi[5)], C.V. Scheel[4a,11)], J.M. Seixas[3,4)], A. Simon[12)], M. Sivertz[1)], P. Sonderegger[4)], M.N. Souza[3)], Z.D. Thomé[3)], V. Vercesi[5)], Y. Wang[6)]†, R. Wigmans[4,11)] and C. Xu[6)]†

1) *University of California, San Diego, USA*
2) *Università di Napoli and INFN Sez. Napoli, Italy*
3) *COPPE/EE/UFRJ, Rio de Janeiro, Brazil*
4) *CERN, Geneva, Switzerland*
4a) *CERN/LAA project, Geneva, Switzerland*
5) *Università di Pavia and INFN Sez. Pavia, Italy*
6) *Worldlab, Lausanne, Switzerland*
7) *LIP, Lisbon, Portugal*
8) *Università di Cagliari and INFN Sez. Cagliari, Italy*
9) *Cornell University, Ithaca, USA*
10) *LPNHE, Université Paris VI&VII, Paris, France*
11) *NIKHEF-H, Amsterdam, the Netherlands*
12) *Universität Heidelberg, Heidelberg, Germany*

† On leave of absence from IHEP Beijing, China

ABSTRACT

The lateral profile of the energy deposition in a prototype of a lead and scintillating fiber calorimeter, constructed in the framework of the LAA project at CERN, has been measured for both electromagnetic and hadronic showers in the energy range from 5 to 150 GeV. The distributions are well described by analytic functions whose parameters allow one to determine the radial scaling of the shower development. In the electromagnetic case, the data are compared to Monte Carlo calculations. Estimates of the lateral leakage outside of the detector are made as well as calculations of the average π^0 content of hadronic showers and event-to-event fluctuations in this electromagnetic component. A method is developed whereby knowledge of the hadronic shower profile can be used to determine the relative calibration constants of neighboring towers in such a calorimeter.

(Submitted to Nuclear Instruments and Methods in Physics Research)

1. Introduction

The Spaghetti Calorimeter (SPACAL) is a lead and scintillating fiber sampling calorimeter, developed within the framework of the LAA project at CERN, that offers the excellent energy resolution, hermeticity, speed, and lateral segmentation necessary for future high energy colliders.[1] Its basic electromagnetic and hadronic calorimetric properties have recently been measured[2,3] in a full-scale (13 ton) prototype, including certain aspects of longitudinal shower development.[4] The structure of the prototype lends itself well to the study of the lateral distribution of the energy deposit from pion and electron showers because of its small lateral cell size. Such measurements are important in determining the relevant shower cluster sizes for a calorimeter operating in a future SSC/LHC experiment, as well as for setting a benchmark against which Monte Carlo code simulating shower development may gauge itself.

The average lateral shape of electromagnetic showers has been examined by many others in a variety of materials (see for example Bathow *et al.*,[5] for measurements made in lead, copper, and aluminum at 6 GeV) and has been shown to agree quite well with Monte Carlo calculations to 2 or 3 orders of magnitude in the energy deposit. Similarly, attention has recently been focused on the measurement of the lateral profile of hadronic showers. Among the latest work include measurements[6] made by the Zeus Calorimeter Group using a uranium/scintillator calorimeter in the energy range from 10 to 100 GeV, and studies[7] made by the WA80 collaboration using an iron/gas calorimeter at energies below 25 GeV. The former offers comparisons with current Monte Carlo simulations of the hadronic shower development process but is limited by coarse segmentation. The latter suffers a suppression of the electromagnetic component of the shower. Neither examines the lateral profile of the energy deposit beyond an energy range greater than about two orders of magnitude.

In this analysis we present data covering nearly 5 decades in the energy deposit out to a radius of 50 cm for a prototype of a lead and scintillating fiber calorimeter. The beam energies for electrons and pions varied from 5 to 150 GeV. The calorimeter is described in section 2, and the data selection is described in section 3. In section 4 we try several phenomenological functions to describe the average lateral energy deposit, and use these functions in section 5 to estimate the shower containment at different radii as well as to estimate the average π^0 fraction of hadronic showers. Section 5 also describes a technique of calibrating the calorimeter using knowledge of the hadronic shower profile. A comparison is made to Monte Carlo calculations for electromagnetic showers.

2. The Calorimeter

The calorimeter used in this analysis has 13 tons of instrumented mass and measures 1 meter in diameter by 2 meters deep. It is read out by 155 longitudinally unsegmented and nonprojective towers that are hexagonal in cross section with an apex to apex distance of 86 mm. The absorber consists of grooved sheets of extruded lead 1.92 mm thick, 50 mm wide, and 2 m long. Plastic scintillating fibers* 1.0 mm in diameter are placed into the 1.1 mm wide grooves lengthwise so that they can be read out at the rear of the detector. The front ends of the fibers have been polished and mirrored with sputtered aluminum (85% reflectivity) to increase the effective attenuation length of the fibers to about 8 m, thereby making the response of the calorimeter more uniform with depth.

The detector was constructed by stacking the lead and fiber matrix without the use of any glue or solder. The fiber to fiber spacing is 2.22 mm and is done in such a way that each fiber is equidistant to its six nearest neighbors (hexagonal geometry, as shown in fig. 1a). Each tower is formed at the rear by bunching 1141 fibers into an hexagonal structure, machining and polishing the end surface, and then coupling the light through an hexagonal light guide (79 mm long, 42 mm apex to apex) to a photomultiplier.**

The lateral cross section of the detector as a whole is shown in fig. 1b. The central tower is surrounded by 6 concentric hexagonal rings and one partially complete ring. The active part of the calorimeter has roughly a cylindrical shape with a diameter of 1 m. By construction, there are no cracks between the towers.

The volume ratio of lead to fiber was set at approximately 4:1 in order to achieve compensation, but subsequent analysis[3] demonstrated that $e/h = 1.15 \pm 0.02$. That is, the π^0 component of hadronic showers will be overestimated by 15% relative to the non-electromagnetic part, and this will have to be accounted for when interpreting the results of the hadronic shower profile. The volume ratio leads to a rather small sampling fraction (2.3% for electromagnetic showers) and compact shower dimensions. The effective radiation length (X_0) of this detector is 7.2 mm, and the effective Molière radius[8] (R_M) is 20 mm. The effective nuclear interaction length[9] (λ_I) is 21 cm while the average density is 9.0 g/cm^3. Therefore, the dimensions of the calorimeter amount to 9.5 λ_I in depth by 4.8 λ_I across.

Two methods were employed to improve the dynamic range of the readout electronics during the test period. On the one hand, the high voltages of the photomultipliers were set to yield gains that gradually increased radially from the center of the detector; on the other, the output of each photomultiplier signal was split into an amplified and

* SCSF-38, produced by Kyowa Gas, now Kuraray Co. Ltd., Tokyo, Japan

** Phillips XP 2282, 8-stage

unamplified channel. Two anode signals were delivered from the base of each SPACAL tower by means of a passive splitter. One of these went into the counting room and was fed into an active splitter to deliver one signal with a gain of 1 and another with a gain of approximately 10. The two signals were digitized by a 12-bit charge-sensitive ADC* operating under a 400 ns gate. The gain of the ADCs was approximately 4 counts/pC for a full scale range of 1000 pC, and sparse data readout was enabled: signals smaller than 4 counts above pedestal value were not recorded.

The other part of the base signal went into a linear adder* to be combined with the signals of each of the towers in the same hexagonal ring. The resulting ring sum signals were then treated identically to the signals that went directly into the counting room. This procedure helped to eliminate some of the effects of the ADC threshold on the signal distribution and will be discussed further in section 3.3. In practice, only rings 3 through 7 were instrumented for this part of the base signal.

The gain of the photomultipliers in the central detector region was set to deliver 4 pC per GeV of electromagnetic energy deposit into each of the two paths leaving the bases. This gradually increased to 20 pC/GeV for the outermost rings so that the ADC threshold for a single tower on an amplified path corresponded to about 5 MeV.

3. Data Selection

3.1 The Beam Line

The measurements presented in this analysis were performed in the H2 beam line of the Super Proton Synchrotron at CERN during June 1990. A trigger counter telescope was employed which consisted of 5 scintillation counters ($S_1 - S_5$) and two beam chambers (BC_1 and BC_2) with x and y readout as shown in fig. 2. A sixth trigger counter (S_6) was often employed 12 cm in front of the calorimeter with an absorber sheet (1.14 X_0 tungsten and 0.53 X_0 lead) strapped upstream to act as a pre-shower detector, and this helped to discriminate between pions and electrons. In addition, a 10 cm thick block of paraffin was sometimes installed in one of two positions in front of the calorimeter with another scintillation counter (S_J) following it in an attempt to simulate hadronic jets. This block was 44 cm upstream of the calorimeter in the close position and 147 cm upstream in the far position. Triggering required a pulseheight in S_J of at least twice the minimum ionizing value. Finally, a smaller prototype of the calorimeter described here, consisting of only 20 towers, was placed *transversely* behind the main calorimeter to detect particles leaking out the rear.

---

* LeCroy 2280 series
* LeCroy 628

Data were taken at beam energies of 5, 9.7, 20, 40, 80, and 150 GeV for electrons and negative pions. The electron beams studied in this analysis were incident at an angle of 3° with respect to the fiber direction, whereas the pion beams were incident at 0°. The 3° tilt is necessary to reduce channeling effects of the electrons.[1] At low beam energies (5 and 9.7 GeV) the pre-shower detector formed part of the trigger and rejected pion events if the S_6 pulseheight was above about 7 times the minimum ionizing value. Electron events were rejected if the S_6 pulseheight was below this value.

The main calorimeter was calibrated at 40 GeV by sending about 1500 electrons into the centers of each of the towers. This gave a statistical precision of about 0.3% on the relation between picocoulombs to GeVs; but because of instabilities in the photomultipliers and local nonuniformities in the response of the fibers, the relative calibration of the towers is known to only several percent. The calibration runs lasted 51 hours for 155 towers.

Approximately 3000 electrons and 5000 pions were sent into the center of the calorimeter at each of the above energies with the pre-shower detector S_6 in place. Furthermore, at 80 GeV a $12 \times 12\text{cm}^2$ electron grid scan and a $24 \times 24\text{cm}^2$ pion grid scan were performed, each consisting of 49 different impact points and about 2000 events at each point. These latter grid scans, performed at an angle of 2° with respect to the fiber direction and without the pre-shower detector, offered great detail on the lateral shower shapes since they provided many different off-center beam impact locations within a tower. A plot of the locations for the electron scan is shown in fig. 3. The spacing for the pion scan was twice as large. Finally, pions at energies of 40, 80, and 150 GeV were sent into the paraffin target, placed either at 44 or 147 cm upstream from the calorimeter, with the S_J counter in the trigger. About 10000 events were recorded at each energy. As with the grid scan, S_6 was removed and the tilt was 2°.

3.2 Analysis Cuts

Offline analysis cuts on the data require that the beam spot, as measured by the beam chambers, lie within a 1 cm radius at high energies (40–150 GeV), within 1.2 cm for 9.7 and 20 GeV, and within 2 cm for 5 GeV electrons. Furthermore, the x and y readout of the two chambers must agree to within 1.3 cm at all energies but 5 GeV to limit the contribution of off-axis events. The cut is 3.2 cm for 5 GeV electrons. Neither cut is applied to 5 GeV pions since other cuts already limit the sample size substantially.

The pulseheights on the two trigger counters S_1 and S_2 are required to be between 0.5 and 1.75 times the minimum ionizing value. To remove events caused by contaminating beam particles, a cut of twice the minimum ionizing value is imposed on the S_6 pre-shower detector when it is in place. Electrons below this cut are rejected, as are pions above it. To further separate between the two particles, and additionally to eliminate possible muon contamination, a containment cut based on the energy deposit pattern in

the main calorimeter is exploited. The fraction f_6 [10] of the energy deposited in the six towers with the largest contribution to the total signal is required to be larger than 98% for electron candidates. Pions are accepted only if they are less contained than this, which removes the electron contamination but more importantly discards the significant muon contamination at low energies. Typically, muons will interact in only one or two towers, and electrons are contained to about 95% in one tower. The effect of this cut is slight at high beam energies.

As it was, the pion (electron) contamination in the electron (pion) beam was minimal ($< 1\%$) at energies above 40 GeV. The muons in the pion beam comprised 2% of the events at 150 GeV, increasing to 80% at 5 GeV. Additional muon rejection is obtained by requiring the backing calorimeter to show less than about 0.1 GeV of energy deposit and by eliminating events that deposit less than 1.75 GeV in the main calorimeter. In all, about 50% of the electron and pion samples survived all the cuts except at 5 GeV where the muon contamination was substantial[4] .

For the simulated hadronic "jet" events, a charged particle multiplicity cut based on the S_J pulseheight is always applied. The cut eliminates events that deliver a signal of less than 9 times the minimum ionizing value.

Initial analysis of the data from this test period showed 8 towers in the main calorimeter to be noisy. For this reason, they are left out of the analysis covered in this paper. If the total signal from the calorimeter is needed, an interpolation for the signals in these towers is made by using the lateral profile fits described in the next section. Three other towers suffered from readout problems and thus did not have the amplified data as described in section 2 available. Consequently, information was not always available from these towers when the energy deposit was smaller than the ADC threshold on the unamplified path.

3.3 Corrections and Limitations

As pointed out in section 2, the readout electronics ignore signals smaller than 4 ADC counts above the pedestal value. This tends to bias the average of the observed signals toward smaller values for the signals observed in the outer rings of the calorimeter (and for those channels without amplified information). Indeed, for towers in the outermost ring, only about 10% of the events have signals above the ADC threshold for 9.7 GeV pion showers. This limitation in the readout distorts the outer shape of the lateral profile, particularly for low energy pion showers.

One method to recover this lost information was described[3] in another paper, and depends on parameterizing the observed signal distribution to estimate what fraction is missing. Specifically, a Poisson-like distribution is fit to the signal lineshape of each tower and the integral of the area below the cutoff is calculated. For the present analysis,

further investigation into the nature of the ADC threshold correction was made since the results of this work depend much more on the effect than the results of previous analyses.

This study is based on a detailed comparison of the hardware ring sum signals to the corresponding software sum of the signals from each tower. Recall that each hexagonal ring had a part of their signals ganged together before entering the ADC, thus increasing the total size of the signal relative to the electronic threshold. Analysis of the available hardware sums on pion data show that their signals are indeed larger than the equivalent software sums of individual towers, indicative of the effects of the cutoffs, with the discrepancy greatest at the lowest beam energies. This is illustrated in fig. 4 for rings 3, 4, and 6 as the total ring sum signal per GeV plotted as a function of the pion beam energy. When one corrects for the limitations in the ADC readout according to the original method of fitting to the lineshape of each tower, one finds that the resulting new software ring sum is too large compared to the hardware sum.

For the present analysis the difference between the software ring sum and the hardware ring sum is taken to be size of the threshold correction for the ADCs. A factor is added to the mean signal of each tower so that the two ring sums agree. In principle this ignores the threshold effect on the hardware sum, but since the signal distribution was well separated from the cutoff this correction is negligible. Possible explanations for why the original method (which predicted a correction roughly twice the difference between the hardware and software ring sums) overestimated the effect are that noise and pedestal fluctuations can distort the signal shape by artificially moving events above the cutoff. Since the electronic signals were always pedestal subtracted, these fluctuations can only increase the observed mean whereas the original effect was to decrease it.

Since this procedure differs from what was previously published[3] one is naturally concerned about how such a change affects the results of earlier work. For instance, the calculation of e/h depended on an estimate of the total amount of signal that goes unobserved, which includes the threshold correction described here as well as an estimate of the amount of lateral leakage from pion showers escaping the calorimeter (described here in Section 5.1). These two estimates are interdependent: an increase in the signal from each tower extrapolates to a larger amount of leakage; and for the earlier reference[3] the excess signal from the threshold correction led to an anomalously large leakage estimate. Instead, the shape of the lateral profile was forced to be the same at low energies as for high, and the leakage was calculated using those parameters. With the present understanding of the ADC threshold correction no such ad hoc procedure is required to estimate the lateral leakage, and the value of e/h remains unchanged at 1.15.

Finally, the reader is reminded that these corrections are only significant at low beam energies and at large radii from the shower axis. They are meant only to be

suggestive of the systematic error on our measurements, and they will always be shown along with uncorrected data. Since electromagnetic showers are contained to a region with a radius smaller than that of the first available hardware ring sum, no correction is applied to electron runs. The fraction $E_{\rm miss}/E_{\rm obs}$ of the total amount of signal that goes unrecorded in the 155 tower collecting area for pions is shown in table 1 as a function of beam energy.

Further limitations in the analysis of the lateral shower shapes have to do with the noncompensation of the calorimeter and with the attenuation length of the fibers. The calorimeter is not quite compensating ($e/h = 1.15$), so pion showers will inherently exhibit nonlinearities (about 5% in the energy range from 5–150 GeV) with respect to the beam energy due to the changing average π^0 fraction. Moreover, hadronic showers penetrate deeper into the calorimeter and suffer less light attenuation than the more forward and well localized electromagnetic showers. This imposes a different calibration constant for pions than for electrons on the relation between the picocoulombs measured by the ADC to the energy deposition in units of GeV. Since the net displacement is about 40 cm between the two types of showers over an attenuation length of about 800 cm, the effect is on the order of 5%. Unfortunately, the average depth of the showers varies with energy. This poses no problem for electromagnetic showers because the scaling distance is a radiation length, but hadronic showers scale with the much larger interaction length and can exhibit small nonlinearities (about 1% per order of magnitude in E) in the observed signal due to light attenuation in the fibers.

The net effect of all this makes a simple calibration of the pion signal independent of the peculiar properties of the calorimeter difficult. Therefore, the pion showers will only be presented in units of picocoulombs, but models will be invoked to understand certain nonlinearities. The interested reader in referred to another paper[3] on how to remove these effects. The lateral electromagnetic profiles will be presented in terms of the measured picocoulombs and the inferred energy deposit (4.0 pC/GeV).

3.4 Shower Axis Determination

A method to obtain the lateral coordinates of a shower axis using the SPACAL calorimeter has previously been reported.[2] Such methods are necessary here to obtain the average position of the shower center since several sets of data used in this analysis have been taken under conditions where the beam does not enter the calorimeter perpendicularly. The finite depth of the shower leads to a lateral shift by several centimeters of the location of the mean energy deposit from the impact position determined by the beam chambers, which is significant compared to the resolution of the lateral distributions. Of course the finite longitudinal extent of the shower also will affect the shape of the lateral profile: any steeply falling core will be broadened somewhat by the tilt of the calorimeter.

The method of obtaining the shower centroid simply involves making an energy-weighted average of the coordinates of the inner 19 towers of the detector. However, because the tower size is comparable to the scaling length of the shower profile in that region, these coordinates must be transformed in a way[2] that is different for pions and electrons.

4. Lateral Shower Shapes

4.1 Fitting Method

The purpose of the analysis in this section is to present the lateral energy distributions of electrons and pions showering in the SPACAL calorimeter and to determine a shower profile function dE/dA that represents the differential energy deposit dE in an infinitesimal area dA of the detector. Analysis of a given run is based on the average signals of the 147 active towers used to collect data. The uncertainty in the energy deposit in a particular tower is taken to be the statistical error on the mean. The finite extent of the beam spot is thus folded into the data: any steeply falling radial dependence of the energy deposit is smeared with the width of the beam. However, shifts in the average location of the shower axis are accounted for as described in section 3.4.

The average shower profile is presumed to depend only on r, the distance from the average shower axis. The data are presented by plotting the mean signal observed in a tower as a function of the distance r from the center of the tower to the average shower axis; thus the differential shower shape is integrated over the surface area of a tower. Although this is a natural way to present the data, one should note peculiarities that exist when not explicitly unfolding the underlying differential profile. For instance, an infinitesimally narrow profile would not lead to a spike in this plot. Rather, for those values of r that were inside the incident tower, the plot would be a constant equal to the energy deposit in that narrow region. An immediate turnover would occur as soon as r reached the boundary of the tower. This explains the rather gentle slope at small values of r in the data to be shown. The steepness in the *differential* profile is only revealed by how quickly this curve turns over as a function of r at the boundary of the incident tower.

In order to compare this data with a phenomenological function, a simplification in the integration is introduced: namely, that the hexagonally shaped towers are approximated by circles of equal area ($r_c = 3.9$ cm). This imposes a negligible error except for beam impacts near the boundary between towers. We assume no leakage out the rear of the detector,[11] so the lateral energy deposit represents an integration over all depths together with the effects of fiber attenuation.

The energy deposited into a tower is calculated to be the integral of a differential shower profile $dE/dA(r)$, for which a certain analytical function is assumed, over the area of a circular tower. For a tower i whose center is located a distance r_i from the shower axis, where $r_i > r_c$, this energy is:

$$E_i = \iint \frac{dE}{dA}\, r dr d\phi = \int_{r_i - r_c}^{r_i + r_c} \frac{dE}{dA}\, r dr \Delta\phi(r) \tag{1}$$

where the angular function is given by:

$$\Delta\phi(r) = 2 \arctan \sqrt{\frac{4 r_i^2 r^2}{(r^2 + r_i^2 - r_c^2)^2} - 1}. \tag{2}$$

Smaller radial impacts logically follow from this.

A χ^2 minimization fit on E_i is done using the MINUIT[12] minimization package to determine the free parameters in the expression to describe $dE/dA(r)$. Only statistical errors on the measured energy deposit are used; but because this method is sensitive to any miscalibration of the towers, these errors are increased to force the χ^2 to equal the number of degrees of freedom before determining the error on any fitted parameter. Typically, the χ^2 values of the fit before scaling range from 10 to 50 per degree of freedom for almost 150 degrees of freedom.

4.2 Electromagnetic Profile

Figure 5 shows the lateral profile of an 80 GeV electromagnetic shower out to 15 Molière radii along with two curves to be described shortly. The data were taken from the grid scan of 49 different impact points, and each dot represents the signal in one tower for one of these positions. As mentioned in section 3.3, no correction is applied to the electromagnetic shower information to account for the effects of the cutoffs of the ADCs. The flat shoulder in the data at radii less than 4 cm is a consequence of containing a narrow shower in a relatively wide tower, a feature already noted in the last section.

The solid line through the data is the result of a calculation based on the EGS4[13] Monte Carlo program. One hundred showers were simulated at 80 GeV using the S-PACAL geometry. Energy cutoffs were 0.1 MeV for electrons and positrons, 0.01 MeV for gammas. The radial energy deposit, as determined by EGS, was satisfactorily parameterized by:

$$\frac{dE}{dA} = \frac{19.70}{r} e^{-r/0.39} + \frac{2.46}{r} e^{-r/1.53} + \frac{0.42}{r} e^{-r/3.00} \quad \mathrm{GeV/cm^2} \tag{3}$$

This radial energy density could then be integrated to yield the signals that would occur in a SPACAL tower as a function of radius. This technique was checked by

directly tallying in EGS4 the energy deposit in the towers of the first few rings of the SPACAL calorimeter; the agreement was good.

The Monte Carlo calculation does a very good job in describing the data for radii less than about 20 cm (10 R_M), and it is remarkable that the agreement extends over 5 orders of magnitude in the energy deposit. The departure of the Monte Carlo from the data at radii greater than 20 cm, where more signal seems to be recorded in the data, is a feature that also was noted by Bathow *et al.*[5] for their measurements made in lead.

The dashed line shown in fig. 5 is a fit of a two-parameter energy density function that is similar to that used by Grindhammer, Rudowicz, and Peters:[14]

$$\frac{dE}{dA} = \frac{A/r}{(r^2 + B^2)^2} \tag{4}$$

Although traditionally a double exponential is used to parameterize the lateral energy deposit, this choice describes the data equally as well, and its two parameters have a much more physical interpretation. The natural scale length B is very close to the Molière radius. Of course, the small r dependence is only approximate: one can see deviations of the fit in the steep region after the shoulder. But for this analysis, a simple global description seems more intuitive than a complicated expression. One can anyway rely on EGS4 to get the expected shape of electromagnetic showers.

This global behavior scales very well with energy. Figure 6 shows the lateral profile of a 9.7 GeV electromagnetic shower taken at one impact point. Note the far fewer data points available than with the grid scan data. In this graph, the first data point is the central tower, the next six are the ring of towers surrounding it, and so on. The solid line is again an EGS4 calculation –this time with 400 simulated showers– and the dashed line is the two-parameter fit. Table 2 and figs. 7a and 7b show the values of these parameters as a function of the beam energy. Parameter A, when divided by the beam energy, is practically independent of energy, at least for $E \geq 20$ GeV. Parameter B is consistent with the Molière radius. Both A and B are positively correlated so that if one fluctuates upwards, the other tends to follow. This explains why at 5 GeV the fit with the lowest χ^2 has both parameters systematically larger than those at other energies. Only the statistical errors on the parameters are shown.

Perhaps a better way to display the energy scaling of the data that is less subject to correlations among the parameters is to divide the signal in each tower by the beam energy and then to display all of the energy scan runs on one graph. This is done in fig. 8. The dashed line is the best fit curve to all of the data, and the result is listed in the last row of table 2.

4.3 Pion Profile

A sample of runs from the 80 GeV pion grid scan is included in fig. 9. Several analytic forms of the differential energy deposit were tried, but the simplest that describes the prominent central core and the surrounding halo is a combination of an exponential and a Gaussian:

$$\frac{dE}{dA} = \frac{B_1}{r} e^{-r/\lambda_1} + \frac{B_2}{r} e^{-r^2/\lambda_2^2}. \tag{5}$$

The solid curve in fig. 9 is a best fit of this function to the pion grid scan data. The central core of the pion shower is seen to have a 4.24 cm scale length while the large r region scales with 14.0 cm. The latter presumably is composed mainly of low energy neutrons released in the shower development process that have rather large scattering lengths. The phenomenological ansatz (5) fits the data rather well over almost 4 decades of variation in energy deposit. Of note is also the slow turnover of the profile at the tower radius, which indicates a much broader lateral energy deposit than an entirely electromagnetic shower.

The correction for the energy cutoff of the ADCs is significant at low energies. Figure 10 shows the lateral shower profile of 9.7 GeV pions without any corrections (open circles) and with a correction based on the technique described in section 3.3 (crosses). At large radii the correction predicts a shallower profile than the uncorrected data suggests, which has implications on the estimated amount of leakage outside of the calorimeter. The scaling length λ_1 of this outer region is 16 cm when eq. (5) is fit to the corrected data (dashed line), but only 14 cm when the uncorrected data are used (solid line).

Table 3 lists the values of the 4 parameters of eq. (5) when fit to data of all energies. The numbers in parentheses refer to the results when corrected data are used, whose statistical errors are comparable to those shown for the uncorrected results. We should point out that the parameters listed for 80 GeV are slightly different than those obtained with the grid scan, particularly λ_2 which describes the central core; but the grid scan was performed with the calorimeter tilted by 2° with respect to the beam so one should expect a slightly broader core. The results listed in table 3 concern pions that enter the calorimeter perpendicularly.

The energy dependence of the scaling parameters λ_1 and λ_2 is displayed in figs. 11a and 11b. The values of λ_1 based on the uncorrected information from the detector are practically constant with beam energy at 14.3 cm. The corrected information shows an increase in λ_1 at energies below 40 GeV up to 17.7 cm at 5 GeV. The value of λ_2 decreases with increasing beam energy, indicating that the central core of the shower is becoming steeper, a situation noted by others.[6] The corrected and uncorrected values lie close to each other for all energies because the limitations in the readout are not significant at small radii.

The energy dependence of the remaining two parameters is plotted in figs. 12a and 12b for the quantities B_1/E and B_2/E. It can be seen that for both uncorrected and corrected data, that B_1 is essentially linear with beam energy and that B_2 increases more than linearly. This can be stated quantitatively as follows for the corrected data:

$$\begin{aligned} B_1 &= 0.021\ E \\ B_2 &= 0.043\ E^{1.2} \end{aligned} \tag{6}$$

The increase of B_2 with energy can be interpreted as a growing electromagnetic component of the hadronic shower development.

Although one does not expect the pion shower shape to scale linearly with energy in this calorimeter for the reasons described in section 3.3, one can anyway treat the profile data that way by dividing the tower signals by the beam energy and displaying all available energies on one graph as was done for the electromagnetic showers. This universal curve is shown in fig. 13 for the uncorrected data only. An expanded view to show the differences in the small r region is shown in fig. 14. The graphs show a large degree of scaling in the pion shower profile from 5 to 150 GeV. The main difference lies in the fraction of the energy deposited into the central tower, which increases with beam energy. This leads to a *decrease* in the percentage of energy lost laterally outside the detector ($r > 50$ cm) with increasing beam energy. Further discussion of this point is deferred until section 5.1. A fit to the energy deposit using the energy density function given by eq. (5) is shown as a solid line through the data points; its parameters are listed in the last row of table 3.

4.4 Multi-particle Profile

Showers initiated by a single hadron actually will be quite rare in experiments at the new multi-TeV colliders such as the SSC and the LHC. More frequent will be the hadronic *jets* that result when the quarks and gluons scattered from the primary interaction fragment into a spray of particles. For that reason, it is important to understand the shower dimensions in a calorimeter planned for one of these new machines when the initiating event is a jet rather than a single pion. In the present analysis, an attempt was made to simulate these high energy multi-particle jets by placing a block of material in the beam line and requiring an interaction to occur as measured by a downstream scintillation counter. Events were selected to have the greatest charged multiplicity available –9.0 or larger– the overflow value of the S_J ADC. We recognize the fact that these "jets" lack the true multiplicity, electromagnetic content, and width of real jets; so this topic needs more study.

Figure 15 is a plot of the lateral shower profile of an 80 GeV "jet" with the target in the close position, 44 cm upstream of the calorimeter. The profile is similar to that from

single pions. The large r scaling length is slightly larger at 15.2 cm as determined by a fit of the energy density function used for single pions. Also, the small r development is slightly different; the central core is noticeably wider and smaller in amplitude. Aside from the 2° tilt of the calorimeter, this is a direct result of the opening angle of the cone of particles leaving the target.

Figure 16 is a plot of an 80 GeV "jet" but with the target moved further upstream to 147 cm. The central core now barely stands out above the periphery. The fit to the data based on the energy density function of eq. (5) does not quite describe the shape of the profile at the smallest radii by overshooting slightly the energy deposit in the central tower; so one really requires a new function to describe the features of the profile. This can be seen in table 4 which lists the values of B_1, B_2, λ_1, and λ_2 when eq. (5) is fit to the lateral profiles of these simulated "jets." The parameters drift away from the single pion ones as the energy decreases and the target is moved away. This is to be expected since the opening angle of the cone of particles–determined by the average $P_T/P_{||}$ of particles produced in the upstream interaction–will increase with decreasing longitudinal momentum; and the projection of this cone on the front face of the calorimeter will increase as the distance between target and the calorimeter increases. The data at 40 GeV with the target in the far position are left out of the table since a fit to the lateral profile could no longer be made to converge.

A less obvious characteristic of these simulated "jets" is that the total energy contained under the lateral profile curve (integrated to infinite radius) is smaller than for single pions. Approximately 7% of the signal for 80 GeV "jets" originating from the far target position is unaccounted for. Two effects will cause such a change. One is that some amount of energy will be lost in the paraffin target because of the energy spent in the recoil and the breaking up the impacted nucleus. The other is that the average depth of the resulting shower in the calorimeter will move forward relative to single pions, and the attenuation of the fibers will reduce the observed signal. It may be convenient to think of the "jets" as hadronic showers with a fixed starting point, namely in the target; whereas single pions penetrate the calorimeter on average by an interaction length (which for pions is approximately 1.5 $\lambda_I = 30$ cm) before interacting, the "jets" do not. A difference in the mean depths of the two types of showers has been inferred from the lateral displacement of the shower centroids with the calorimeter tilted, and confirms about a 30 cm shift. This leads to a 3-4% effect from the attenuation of the fibers.

5. Applications

5.1 Containment Studies

We turn now to a study of how the shower shapes determined in the last section translate into cluster sizes for our detector. The parameterizations of the lateral energy deposit based on eqs. (4) and (5) can be integrated to yield the shower containment as a function of radius. Taking 80 GeV as a standard energy, fig. 17 shows the containment fraction of electrons, pions, and hadronic "jets" as a function of the radius of the cluster size. The latter is taken with the target 147 cm upstream of the detector.

The figure shows that electromagnetic showers are 95% contained in a cylinder of radius 3.5 cm (1.8 R_M) and 99% contained in a radius of 6.5 cm (3.3 R_M). For the current prototype this corresponds to one tower and a group of 7 towers respectively. Hadronic showers initiated by a single pion are only 50% contained in a region of radius 3.5 cm (0.17 λ_I), and they are contained to the 95% level in a radius of 32 cm (1.5 λ_I), which is roughly equivalent to the inner 61 towers of this detector. The "jets" are less contained. The model chosen here selects the target 147 cm from the calorimeter and requires a charged multiplicity of 9 or greater in each event. At a radius of 11 cm (0.53 λ_I) these showers are 50% contained, and at a radius of about 50 cm (2.5 λ_I) they are 95% contained.

The energy dependence of the containment was also studied by estimating the lateral leakage outside of the calorimeter for showers initiated by a single pion. This method involves extrapolating the shower profile curve based on eq. (5) to infinite radius from the boundary of the calorimeter (at an effective radius of 49 cm). The resulting leakage as a fraction of the total signal is shown in fig. 18 for both uncorrected data and data corrected for the cutoffs of the ADCs. A significant systematic uncertainty is seen at the three lowest energies, evident by the departure of the corrected data from the uncorrected, which is a direct consequence of the uncertainty in the slope of the shower profile near the outside edge of the calorimeter. The 5 GeV adjusted data are a factor of 3 larger (3% versus 1%) than the uncorrected data. The two curves drawn through the points are based on simple estimates of the non-electromagnetic component of pion showers, and they will be treated in detail in the next section. We remark here that the fractional energy loss is smaller at high energy than at low energy.

5.2 π^0 Content of Hadronic Showers

Of interest in the study of the hadronic shower development process is a measure of the fraction of energy that is bled off into electromagnetic channels. This fraction, primarily composed of π^0s which are produced in the first few generations of the shower development, has previously been studied using Monte Carlo code for hadronic interactions (*cf.* ref. 15 and the references therein). In the present analysis, an ansatz is made based on the lateral shower development to calculate this quantity using the data available from this calorimeter.

An estimate of the average π^0 fraction can already be inferred from the energy dependence of the ratio of the electron signal to the pion signal ("e/π"). If "e" denotes the efficiency in converting electromagnetic energy into a measureable signal, and "h" the same for non-electromagnetic energy, then

$$\frac{e}{\pi}\left(E\right) = \frac{e/h}{(e/h-1)f_{\pi^0}(E)+1} \tag{7}$$

where f_{π^0} is the average fraction of energy going into π^0 production in an hadronic shower. By measuring the energy dependence of e/π one can infer e/h and f_{π^0}. This was done in a previous analysis[3] to yield $e/h = 1.15 \pm 0.02$.

Another method of determining f_{π^0} is to use the lateral shower profile information. If one assumes that the scaling of the hadronic shower at large radii is non-electromagnetic (composed of neutrons, for instance), then one can define that scaling to be the non-e.m. component at all radii. In the present context this means defining $(B_1/r)e^{-r/\lambda_1}$ in the energy density given by eq. (5) to be the hadronic piece. The electromagnetic piece is then the Gaussian term. The fraction of the energy spent in π^0 production based on the parameters of eq. (5) is then:

$$f_{\pi^0}(\text{obs.}) = \left[1 + \frac{2}{\sqrt{\pi}}\frac{B_1\lambda_1}{B_2\lambda_2}\right]^{-1}. \tag{8}$$

A graphical example of how this technique works is shown in fig. 19 for the lateral shower profile of 150 GeV pions. The area above the dashed line is defined to be the electromagnetic fraction of the energy deposit, and it comes out to be 57% of the total. The fact that the exponential non-e.m. term does not show up as a straight line on this logarithmic plot is due to the integration of the differential shower density over the finite area of a tower. In practice there are correlations among the 4 parameters of eq. (5) which might skew the calculation, so λ_1 and λ_2 are held fixed to the values obtained from the universal fit of fig. 13: 14.1 cm and 3.83 cm respectively. The relative amounts of the two pieces in eq. (5) are allowed to vary, however, so B_1 and B_2 are fit to the

pion shower profile at each energy. The calculated electromagnetic fraction is displayed in fig. 20 along with the statistical uncertainties for data uncorrected and corrected for the effects of the ADC thresholds.

Of course, the fact that this calorimeter is slightly undercompensating means that we will overestimate the electromagnetic fraction of the hadronic shower development somewhat. The observed π^0 fraction is related to the intrinsic fraction by the relation:

$$f_{\pi^0}(\text{obs.}) = \frac{(e/h)f_{\pi^0}}{(e/h-1)f_{\pi^0}+1}. \tag{9}$$

One can see that the two are identical when $e/h = 1.0$, but for $e/h = 1.15$ the intrinsic π^0 fraction is reduced to 54% at 150 GeV.

Both Groom[15] and Wigmans[16] have analytic forms for the intrinsic π^0 fraction based on heuristic arguments of the shower development process. Groom's form follows a simple power law:

$$f_{\pi^0} = 1 - \left(\frac{E}{E_0}\right)^{m-1} \tag{10}$$

with the energy scale $E_0 \approx 1$ GeV and $m \approx 0.85$. Wigmans treats the π^0 production logarithmically:

$$f_{\pi^0} = \kappa \ln E \tag{11}$$

with $\kappa \approx 0.1$. The first equation avoids unphysical results at ultrahigh energies, but both break down near 1 GeV. However, both do equally as well in describing calorimeter data in the energy range at which our detector was tested. The two curves in fig. 20 represent fits of eq. (9) to the observed π^0 fraction using both analytic forms given by eqs. (10) and (11). The compensation factor is set at $e/h = 1.15$ and the energy scale is fixed at $E_0 = 1$ GeV. For the power law dependence of f_{π^0} (solid line), $m-1$ comes out to be -0.16. The fit using the logarithmic form of f_{π^0} (dashed line) indicates $\kappa = 0.12$. Both descriptions can be seen to do a fair job at describing the data shown in fig. 20.

With the assumption that the energy deposit at large radii is non-electromagnetic, it is possible to describe the lateral leakage outside of the calorimeter with parameterizations involving eqs. (10) and (11) for the intrinsic π^0 fraction. This is the basis for the two curves drawn in fig. 18. Up to a multiplicative constant C, the fractional leakage f_{leak} can be described by:

$$f_{\text{leak}} = C\frac{1-f_{\pi^0}}{(e/h-1)f_{\pi^0}+1}. \tag{12}$$

Using the two forms for f_{π^0} along with the parameters determined by the fit to the observed π^0 fraction, we are left with only one parameter to scale the height of each

curve in fig. 18. It is remarkable that only the data corrected for the ADC cutoffs exhibit the energy dependence predicted by the above relation.

Sofar, the information extracted from the lateral shower profiles concerns the *average* properties of the hadronic showers. For understanding the calorimetric properties of the detector, and in particular its energy resolution, also the event-to-event fluctuations are very important. In an earlier study[3] , we already investigated the effects of fluctuations in the lateral shower leakage on the hadronic energy resolution. In addition to the average value of f_{π^0}, also the event-to-event fluctuations in the e.m. shower component are important, especially for understanding the effects of noncompensation on the resolution for hadron and jet detection. These fluctuations have to our knowledge never been measured before. They can be roughly estimated by exploiting the fine lateral granularity of this calorimeter and the greatly different lateral profiles of the e.m. and non-e.m. shower components. We analyzed showers induced by pions entering the calorimeter perpendicularly ($\theta_z = 0^0$) in the center of the central tower for this purpose. The π^0 component of these showers is largely contained in this tower, with a small spill-over in the neighboring six towers (see fig. 19), while the "contamination" by the non-e.m. component is small.

Table 5 shows that the fractions of the shower energy contained in the central tower (f_1) are not very different from the values of f_{π^0} derived from the full shower profiles. In particular, the observed energy dependences of f_1 and f_{π^0} are very similar. It should be noted that in calculating f_1, the total calorimeter signal in the denominator was corrected for the (small) effects of lateral shower leakage (see table 1) and other instrumental effects (sect. 3). However, the numerator was not corrected for the small contribution of the non-e.m. shower component to the signal from the central tower and for the spill-over of e.m. energy into neighboring towers. In spite of this, f_1 is apparently a reasonable measure for f_{π^0} and fluctuations in f_1 may be expected to give an indication of the event-to-event fluctuations in the π^0 production in the hadronic showers. As illustrated in fig. 21, these fluctuations are clearly non-Gaussian, especially at high energies. Table 5 lists the RMS widths of the f_1 distributions. The relative width $\sigma_{\mathrm{RMS}}(f_1)/f_1$ is shown as a function of the pion energy in fig. 22. The fluctuations do get smaller at increasing energy, but the improvement is much slower than the $1/\sqrt{E}$ behavior characteristic for many other aspects of calorimetry. It turns out that a logarithmic dependence gives a good description of the data in the energy range from 10-150 GeV. At least part of the deviation observed at the 5 GeV point could have an instrumental origin. The beam spot at 5 GeV is much larger than at the other energies. It is larger than the size of one calorimeter tower. This increases the fluctuations in the fraction of the shower energy contained in this tower.

5.3 Calibration

A bottleneck in the implementation of many calorimeters for the next generation of colliders is the calibration of the massive number of required towers. Placing each of the tens of thousands of calorimeter towers into an electron testbeam could take years. In this section we describe a method of calibration accurate to within 10% that applies the general lateral shape of *pion* showers in the SPACAL calorimeter to reduce the amount of calibration time spent in the testbeam by up to a factor of ten, and it should be applicable to any calorimeter with fine lateral segmentation.

The technique exploits the large lateral dimensions of hadronic showers. Rather than illuminating the calorimeter with an electromagnetic probe whose width is less than the typical size of a tower, one may choose, instead, pion showers which can effectively probe out to a distance of 30 cm away from the impact point. Then one can compare the response of each tower as a function of its distance from the shower axis to the known lateral profile of a pion shower of comparable energy. From the deviation of each tower's signal from the known general shape of the shower, a set of relative calibration constants can be obtained.

To test the method offline, the 155 towers in the calorimeter were purposely miscalibrated, on average by factors of two by generating random multiplicative constants C that were thrown according to a Gaussian in $\ln C$ with a mean of zero and a sigma of $\ln 2$. Data were then analyzed under the conditions outlined in section 3.2. The events analyzed are a sample of 12 runs from the 80 GeV pion grid scan taken along the outer perimeter of the matrix. For each impact point a lateral profile is obtained from the average tower signals, and a fit of the energy density function derived for the pion grid scan (fig. 9) is made to the data. Both λ_1 and λ_2 are fixed in the parameterization at 14.0 and 4.24 cm respectively. Furthermore, the ratio B_2/B_1 is fixed at 4.01, but the overall magnitude of the shower is free to vary. Also free to vary are the average coordinates of the shower axis so that exact positions are not required.

A first pass at the data for one of the impact points is shown in fig. 23. The scatter in the data from the miscalibration is clearly visible, and the curve describes the new best fit of the energy density function. A new calibration constant is defined to be the ratio of the signal predicted by the fit to the measured signal for a tower. These ratios are then averaged for all of the 12 impact points and then applied to the next pass at the data. This procedure was iterated three times and the final result is shown in fig. 24 for the same run as before. The convergence of the method is quite dramatic as the scatter of the data about the curve has been greatly reduced. The centroids of the showers are also in agreement with those obtained before the miscalibration.

Central to the practicality of this procedure is how close the new set of calibration constants come to the old, and how uniform the response of the detector becomes.

Parenthetically we should remark that modules 4, 24, and 31, for which only unamplified data were available, were left out of the procedure because of difficulties in handling the cutoff effects of the ADCs. The new constants have an RMS spread of 15% about the old (obtained with 40 GeV electrons–see sec. 3.1–and not known to better than several percent anyway); however, the spread is only 10% for the inner 37 towers, indicating that the precision of the technique degrades at the largest radii where the signals are smallest. A previous analysis[3] showed that the variations in the response of the calorimeter over all of the impact points in the 80 GeV electron grid scan had an RMS spread of 3%. Using the new calibration constants, this spread increases slightly to 4%; but the area of the scan is limited to the inner 7 towers only.

Interestingly enough, the energy resolution for pions improves at the highest energies from 4.9% at 150 GeV to 4.6%. Since hadronic showers spread over many towers, this is an indication that the new calibration constants are not significantly worse than before. The largest contributing factor to this improvement is the reduction of the response of the central region of the detector. The measured e/π response of the detector drops 3% relative to before at each energy and yields a 4% decrease in the measured π^0 fraction using the techniques from the previous section. As has been noted,[3] a 15% decrease in the central detector region does improve the hadronic energy resolution by 5% because it artificially removes the noncompensation of the detector. The calibration change here, however, is not quite as large and may suggest a slight miscalibration of the central tower.

Finally, although not dramatic, a calibration of this calorimeter accurate to within 10% was accomplished with a data sample much smaller than the electron sample that was used initially; so even just the reduction in the amount of testbeam time required would be a substantial savings for the installation of any future large calorimeter.

6. Summary

We have presented results on the average lateral development of the energy deposition from electromagnetic and hadronic showers in a prototype of a lead and scintillating fiber calorimeter. The electromagnetic shower profile is seen to agree quite well with EGS4 calculations over 5 orders of magnitude in the energy deposit, and it can be very simply described by the Molière radius and one additional parameter. Hadronic showers initiated by a single pion are very well parameterized by the sum of an exponential and a Gaussian, with the scaling length of the former at about 14 cm. The lateral profile of a shower initiated by many particles –"jets"– can be parameterized in the same way, albeit that the Gaussian core is less pronounced and the exponential slope is less steep than for single pions. The average π^0 fraction of hadronic showers can be estimated using the lateral shower profile, and at 150 GeV this fraction is 54% when corrected

for the small undercompensation of the calorimeter. The event-to-event fluctuations in the π^0 fraction decrease much more slowly than $1/\sqrt{E}$ as a function of the pion energy. Between 10 and 150 GeV, a logarithmic energy dependence is observed. Finally, a calibration scheme based on the lateral energy deposit of pion showers has been used to roughly calibrate the towers in this prototype using a minimal amount of information and only slightly degrading the performance of the calorimeter.

ACKNOWLEDGEMENTS

We are deeply grateful to the LAA Project Leader, Prof. A. Zichichi, for his vision, his warm interest and his encouraging support. We thank our colleagues from the UA2 Group, and in particular P. Jenni and L. Mapelli, who helped us in many ways, in particular during the beam tests. The work described in this paper would have been impossible without the outstanding technical support provided by our technicians O. Barnaba, C. Baudoin, M. Borriello, S. Bricola, J.-M. Chapuis, C. Farella, B. Foligne, A. Freddi, G. Improta, G. Iuvino, F. Pagano, S. Robinson, R. Rocco, L. Rose-Dulcina, G. Sannier, C. Schillinger, A. Sigrist and V. Vanzanella. Financial support from the Stichting for Fundamenteel Onderzoek der Materie to the NIKHEF group, from the Istituto Nationale di Fisica Nucleare to the Cagliari, Napoli and Pavia groups, from the Junta Nacional de Investigação Científica of Portugal to the Lisbon group, from the Conselho Nacional de Desenvolvimento Cientifico e Tecnologico of Brazil to the Rio de Janeiro group and from the U.S. Department of Energy and National Science Foundation to the San Diego group is acknowledged. Two of us (S.B. and F.R.) wish to thank the Digital Equipment Corporation for support. And finally, we are grateful to the staff of the SPS, and in particular to N. Doble, for the excellent beam conditions and assistance provided during our tests.

REFERENCES

1. D. Acosta *et al.*, Nucl. Instr. and Meth. **A294** (1990) 193.
2. D. Acosta *et al.*, Nucl. Instr. and Meth. **A305** (1991) 55.
3. D. Acosta *et al.*, Nucl. Instr. and Meth. **A308** (1991) 481.
4. D. Acosta *et al.*, Nucl. Instr. and Meth. **A309** (1991) 143.
5. G. Bathow *et al.*, Nucl. Phys. **B20** (1970) 520.
6. F. Barreiro *et al.*, Nucl. Instr. and Meth. **A292** (1990) 259.
7. M. Catanesi *et al.*, Nucl. Instr. and Meth. **A292** (1990) 97.
8. The critical energy (E_c) that goes into the definition of R_M is taken from O. Dovzhenko and A. Pomanskiĭ, Soviet Phys. JETP **18** (1964) 187, for each material in the calorimeter. The corresponding radiation length is from Y. Tsai, Rev. Mod. Phys. **46** (1974) 815.
9. We define the *nuclear interaction length* λ_I in the same way as the Particle Data Group in Phys. Lett. **B239** (1990), page III 5,6. It is the mean free path for *protons* between inelastic interactions.
10. See further discussion of this cut in Ref. 3.
11. Less than 0.5% energy leakage for 150 GeV incident pions is reported in Ref. 4.
12. F. James and M. Roos, Comput. Phys. Commun. **10** (1975) 343.
13. W. Nelson, H. Hirayama and D. Rogers, SLAC-Report-265 (1985).
14. G. Grindhammer, M. Rudowicz, and S. Peters,"The Fast Simulation of Electromagnetic and Hadronic Showers", *Proceedings of the Workshop on Calorimetry for the Supercollider,* R. Donaldson and M. Gilchriese (eds.), Tuscaloosa, Alabama (1990).
15. D. Groom, "Energy Scaling of Low-Energy Neutron Yield, the e/π Ratio, and Hadron Response in a Calorimeter", *Proceedings of the Workshop on Calorimetry for the Supercollider,* R. Donaldson and M. Gilchriese (eds.), Tuscaloosa, Alabama (1990).
16. R. Wigmans, Nucl. Instr. and Meth. **A265** (1988) 273.

FIGURE CAPTIONS

1. Detail of the front face of the calorimeter (a), and the lateral structure of the detector as a whole (b).
2. The layout of the beam line showing the relative positions of the calorimeters, beam chambers, trigger counters, pre-shower detector, and target positions.
3. Location of the impact points for the electron grid scan. The pion grid scan covers an area twice as large with the same number of points as for the electron case.
4. A comparison of the ring sum signals per GeV obtained from the hardware sum and the equivalent software sum as a function of beam energy for rings 3, 4 and 6.
5. Lateral shower profile for 80 GeV electrons entering the calorimeter at an angle of $\theta_x = 2°$, obtained by combining all of the runs from the grid scan. The average energy deposited in a tower is plotted as a function of the distance between the tower center and the axis of the shower. The solid curve is a calculation based on EGS4, and the dashed curve is a best fit to the energy density function given by eq. (4) (see text).
6. The lateral shower profile for 9.7 GeV electrons showing a calculation based on EGS4 (solid curve) and the result of a fit to eq. (4) (dashed curve), for $\theta_x = 3°$.
7. Energy dependence of the quantities A/E (a) and B (b) where A and B are defined by eq. (4).
8. Lateral shower profile for electrons of all available energies obtained by dividing the average signal in each tower by the beam energy, for $\theta_x = 3°$. The dashed curve is a best fit of eq. (4) to the data.
9. Lateral shower profile for 80 GeV pions entering the calorimeter at an angle of $\theta_x = 2°$, obtained by combining a sample of the runs from the grid scan. The solid curve is a best fit of eq. (5) to the data.
10. The lateral shower profile for 9.7 GeV pions showing both the uncorrected data (open circles) and the data corrected for the cutoff of the ADCs (crosses), for $\theta_x = 0°$. The solid line is a best fit of eq. (5) to the uncorrected data, while the dashed line is the same for the corrected data.
11. Energy dependence of the parameters λ_1 (a), and λ_2 (b) as defined by eq. (5). The uncorrected data are shown with open circles; the corrected, with diamonds.
12. The quantities B_1/E (a) and B_2/E (b) with B_1 and B_2 from eq. (5), as a function of beam energy. The uncorrected data are shown with open circles and the corrected data with diamonds. The curves represent the results of best fits to a proportional (a) or power law (b) dependence on the beam energy.

13. Lateral shower profile for pions from 5–150 GeV obtained by dividing the average signal in each tower by the beam energy, for $\theta_z = 0°$. The solid curve is a best fit of eq. (5) to the data.

14. An expanded view of fig. 13 to show the shower profile differences at small r.

15. Lateral shower profile for 80 GeV "jets" simulated by placing a block of paraffin 44 cm upstream of the calorimeter, for $\theta_z = 2°$. The solid line represents a best fit of eq. (5) to the data.

16. Lateral shower profile for 80 GeV "jets" simulated by placing a block of paraffin 147 cm upstream of the calorimeter, for $\theta_z = 2°$. The solid line represents a best fit of eq. (5) to the data.

17. Shower containment as a function of radius for 80 GeV electrons, pions, and "jets" (147 cm position) as calculated from lateral profile fits. For the electrons use the left-hand scale, for pions and "jets" use the right-hand scale.

18. The estimated lateral leakage outside of the calorimeter for pion showers as a function of beam energy. Both uncorrected data (open circles) and corrected data (diamonds) are shown, along with two fits described in section 5.2.

19. The lateral shower profile for 150 GeV pions showing an extrapolation of the non-electromagnetic piece (dashed line) defined to be just the first term in eq. (5). The relative areas are 57% for electromagnetic and 43% for non-electromagnetic energy.

20. The estimated π^0 fraction of hadronic showers in the SPACAL calorimeter as a function of the pion energy, as determined by the method described in the text. The two curves are calculations taking into account the noncompensation of the detector (see text).

21. The fraction of the shower energy contained in the central calorimeter tower, for 150 GeV pions entering the center of this tower perpendicularly ($\theta_z = 0^0$).

22. The relative width $\sigma_{\mathrm{RMS}}(f_1)/f_1$ of the fraction of the hadronic shower energy contained in the central tower of the calorimeter as a function of the shower energy. The point at 5 GeV was not included in the fit. Data for pions entering this tower perpendicularly in its center.

23. The lateral shower profile of one of the impact points in the pion grid scan after miscalibrating all 155 towers. The curve is a best fit of eq. (5) using some of the parameters determined earlier. It is used to calculate a new set of calibration constants.

24. The lateral shower profile of the same run as in fig. 23 after the calibration scheme described in the text was iterated three times.

TABLE CAPTIONS

1. The fraction $E_{\rm miss}/E_{\rm obs}$ of the total recorded signal that goes unobserved due to the threshold of the ADCs as a function of the pion beam energy.
2. The parameters of the electromagnetic energy density function given by $dE/dA = \frac{A}{r}/(r^2 + B^2)^2$ as a function of energy for $\theta_z = 3°$. The last row represents a fit to all data when divided by the beam energy.
3. The parameters of the hadronic energy density function given by $dE/dA = B_1 e^{-r/\lambda_1}/r + B_2 e^{-r^2/\lambda_2^2}/r$ for pion showers as a function of energy for $\theta_z = 0°$. The numbers in parentheses refer to data that have been corrected for the energy thresholds of the ADCs. The last row represents a fit to all data when divided by the beam energy.
4. The parameters of the hadronic energy density function given by $dE/dA = B_1 e^{-r/\lambda_1}/r + B_2 e^{-r^2/\lambda_2^2}/r$ for "jet" induced showers as a function of energy for $\theta_z = 2°$. Column 2 lists the position of the target forward of the calorimeter.
5. The electromagnetic component of hadronic showers. Listed are the pion energy, the π^0 fraction derived from the lateral shower profile before and after correction for the effects of the ADC threshold, the fraction f_1 of the energy deposited in the central calorimeter tower and the relative width of the f_1 distribution. See text for details.

TABLE 1	
E (GeV)	$E_{\text{miss}}/E_{\text{obs}}$
5	0.049
9.7	0.023
20	0.008
40	0.003
80	0.001
150	–

TABLE 2		
E (GeV)	A (pC-cm^3)	B (cm)
150	931 ± 14	2.00 ± 0.01
80	493 ± 8	1.97 ± 0.01
40	241 ± 4	1.96 ± 0.01
20	121 ± 4	1.96 ± 0.02
9.7	67 ± 2	2.09 ± 0.02
5	40 ± 2	2.19 ± 0.03
all	$(6.18 \pm 0.06)E$	1.98 ± 0.01

TABLE 3				
E (GeV)	B_1 (pC/cm)	λ_1 (cm)	B_2 (pC/cm)	λ_2 (cm)
150	2.86 ± 0.06 (2.85)	14.3 ± 0.2 (14.4)	17.20 ± 0.38 (17.20)	3.63 ± 0.05 (3.64)
80	1.66 ± 0.04 (1.65)	14.3 ± 0.2 (14.5)	7.98 ± 0.18 (7.98)	3.80 ± 0.05 (3.81)
40	0.86 ± 0.02 (0.83)	14.3 ± 0.2 (14.7)	3.61 ± 0.09 (3.63)	3.91 ± 0.07 (3.94)
20	0.46 ± 0.01 (0.43)	14.6 ± 0.2 (15.5)	1.53 ± 0.04 (1.55)	3.95 ± 0.08 (4.03)
9.7	0.22 ± 0.01 (0.20)	14.1 ± 0.1 (16.0)	0.67 ± 0.02 (0.68)	4.08 ± 0.12 (4.22)
5	0.09 ± 0.01 (0.07)	13.5 ± 0.8 (17.7)	0.20 ± 0.02 (0.21)	7.71 ± 0.54 (7.68)
all	$(0.0209 \pm 0.0003)E$	14.1 ± 0.1	$(0.092 \pm 0.001)E$	3.83 ± 0.04

TABLE 4					
E (GeV)	Target (cm)	B_1 (pC/cm)	λ_1 (cm)	B_2 (pC/cm)	λ_2 (cm)
150	44	3.38 ± 0.10	14.4 ± 0.2	8.35 ± 0.36	5.54 ± 0.16
80	44	1.88 ± 0.07	15.2 ± 0.3	2.86 ± 0.14	7.18 ± 0.23
40	44	0.93 ± 0.03	16.7 ± 0.3	0.86 ± 0.05	9.03 ± 0.25
150	147	3.42 ± 0.14	17.0 ± 0.4	3.91 ± 0.19	8.79 ± 0.28
80	147	1.60 ± 0.16	20.7 ± 1.1	1.13 ± 0.12	12.7 ± 0.7

TABLE 5				
E (GeV)	f_{π^0} uncorr.	f_{π^0} corr.	f_1	$\sigma_{\mathrm{RMS}}(f_1)/f_1$
5	0.438	0.327	0.345	0.597
10	0.426	0.393	0.475	0.309
20	0.432	0.418	0.495	0.289
40	0.500	0.495	0.539	0.243
80	0.525	0.523	0.563	0.208
150	0.591	0.566	0.601	0.176

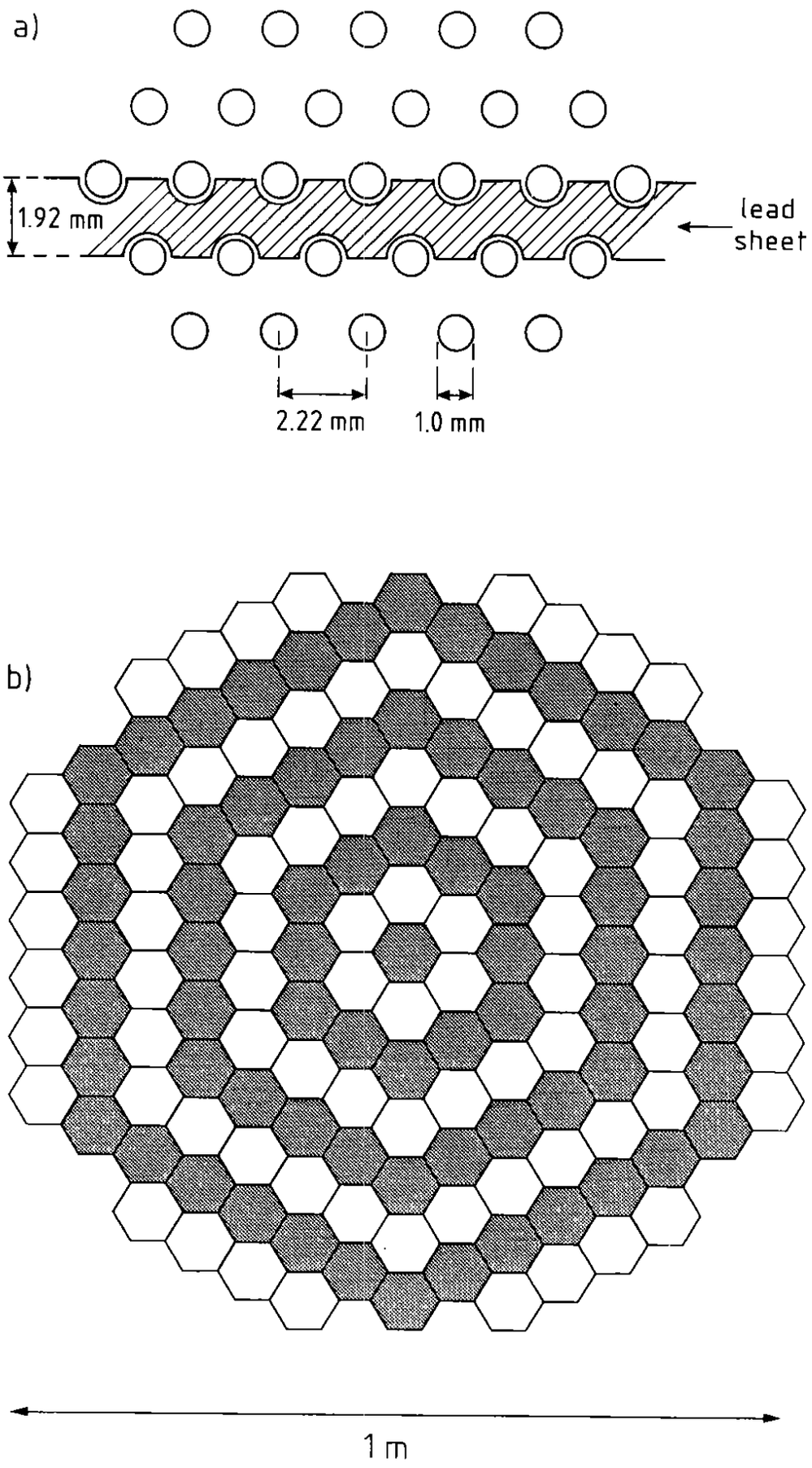

Fig. 1

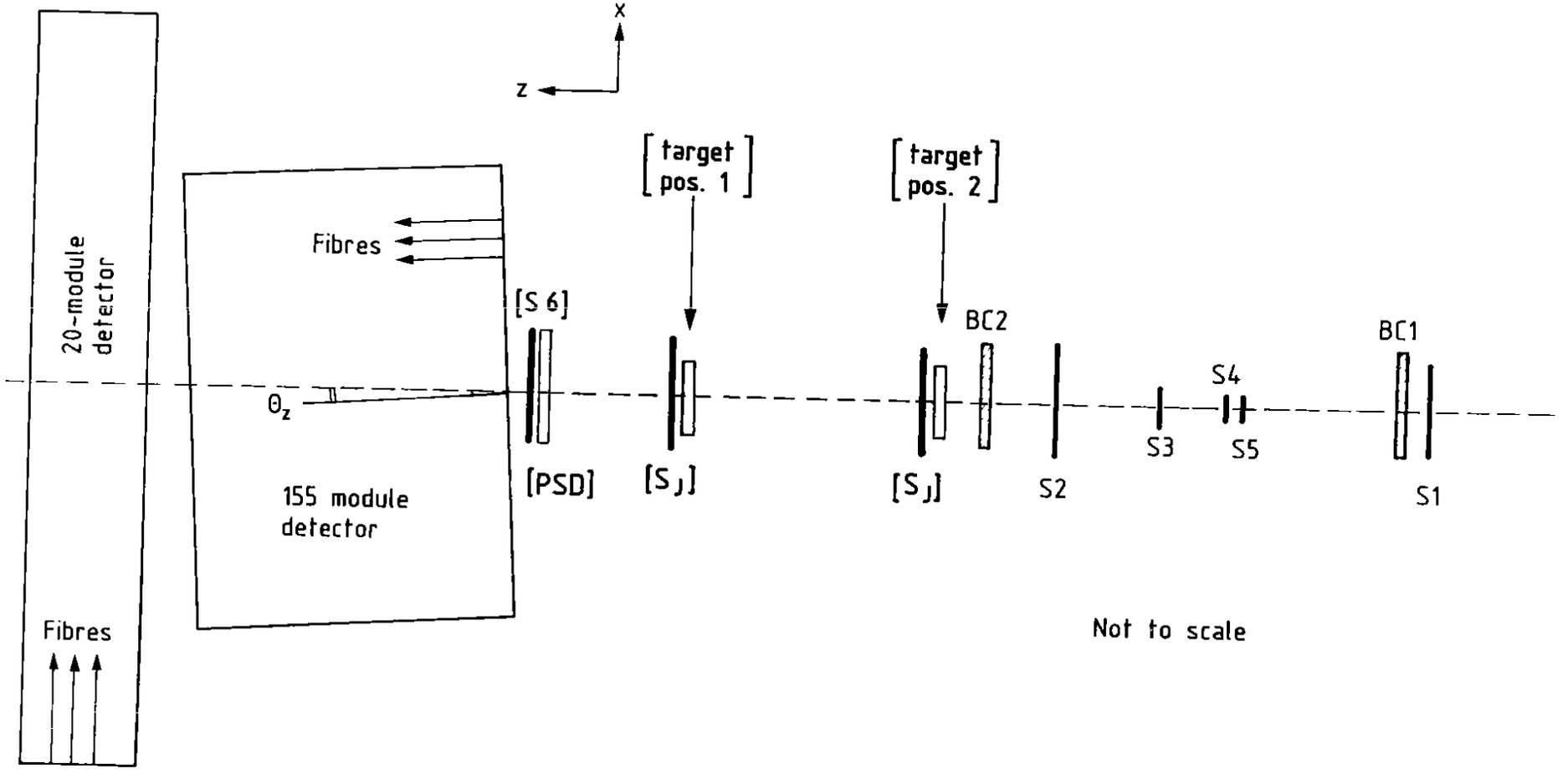
x
z
20-module detector
Fibres
Fibres
155 module detector
θ_z
[S 6]
[PSD]
[target pos. 1]
[S_J]
[target pos. 2]
[S_J]
BC2
S2
S3
S4
S5
BC1
S1
Not to scale

Figure 2

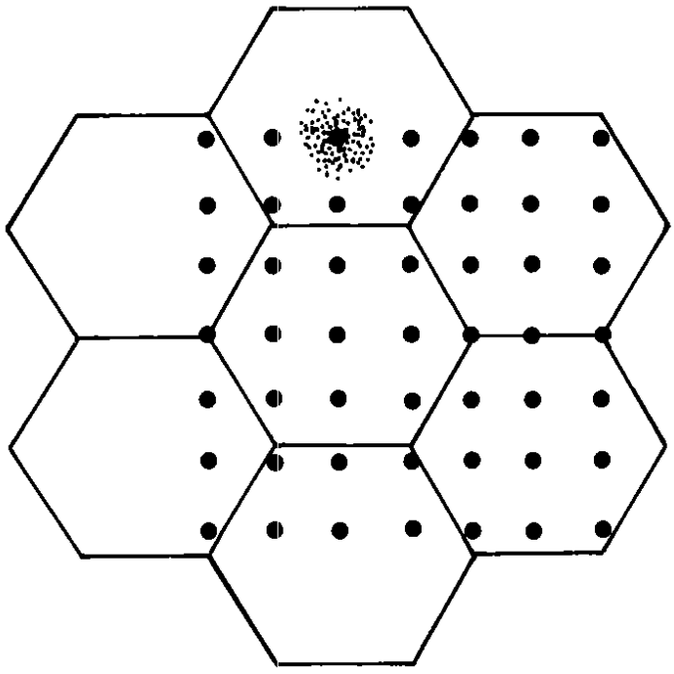

Fig. 3

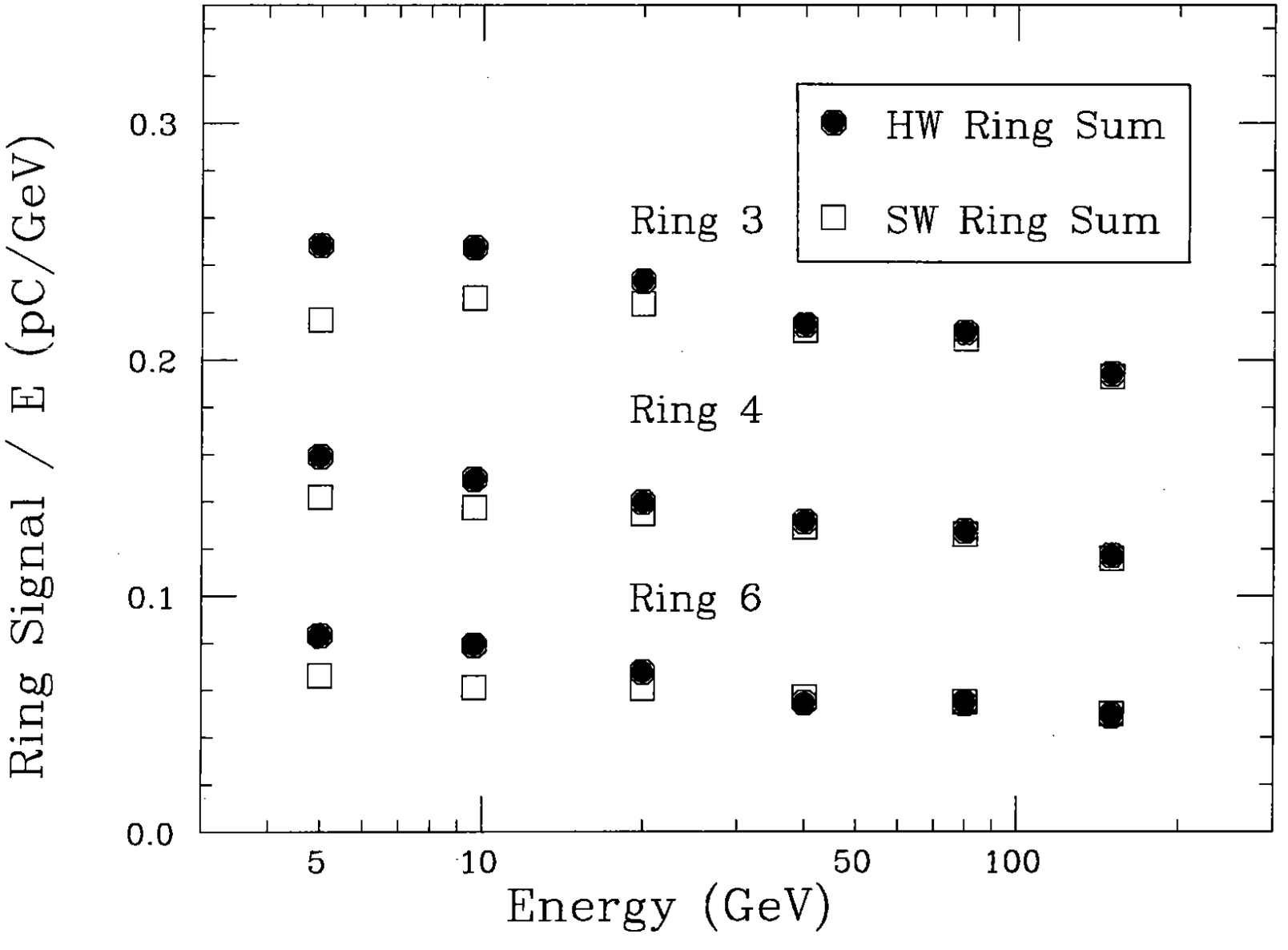
Ring Signal / E (pC/GeV)
0.0
0.1
0.2
0.3
5
10
50
100
Energy (GeV)
HW Ring Sum
SW Ring Sum
Ring 3
Ring 4
Ring 6

Figure 4

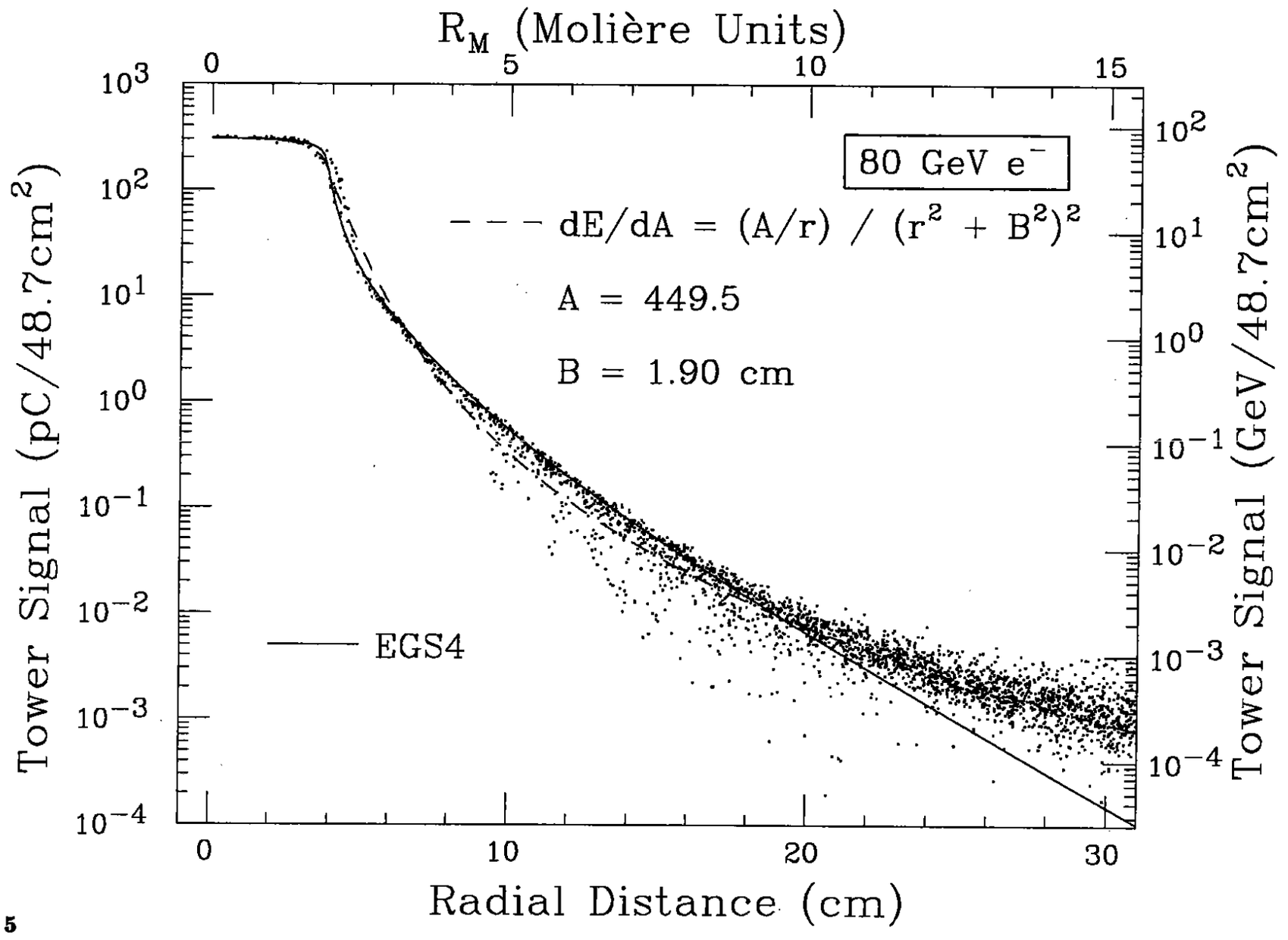
R_M (Molière Units)
0
5
10
15
80 GeV e⁻
dE/dA = (A/r) / (r² + B²)²
A = 449.5
B = 1.90 cm
EGS4
Tower Signal (pC/48.7cm²)
Tower Signal (GeV/48.7cm²)
Radial Distance (cm)
0
10
20
30
10³
10²
10¹
10⁰
10⁻¹
10⁻²
10⁻³
10⁻⁴

Figure 5

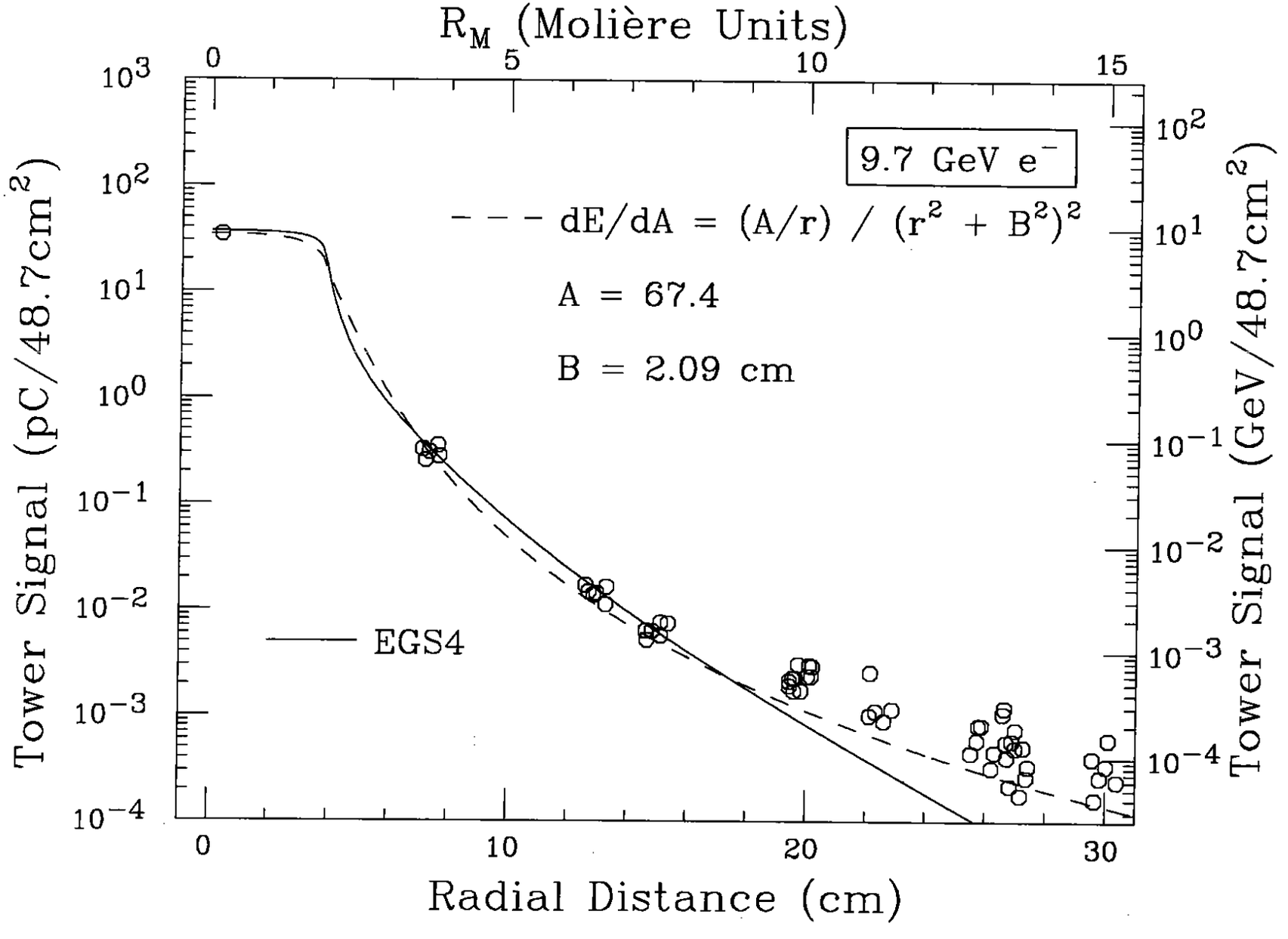
R_M (Molière Units)
0
5
10
15
9.7 GeV e⁻
dE/dA = (A/r) / (r² + B²)²
A = 67.4
B = 2.09 cm
EGS4
Tower Signal (pC/48.7cm²)
Tower Signal (GeV/48.7cm²)
Radial Distance (cm)
0
10
20
30
10³
10²
10¹
10⁰
10⁻¹
10⁻²
10⁻³
10⁻⁴

Figure 6

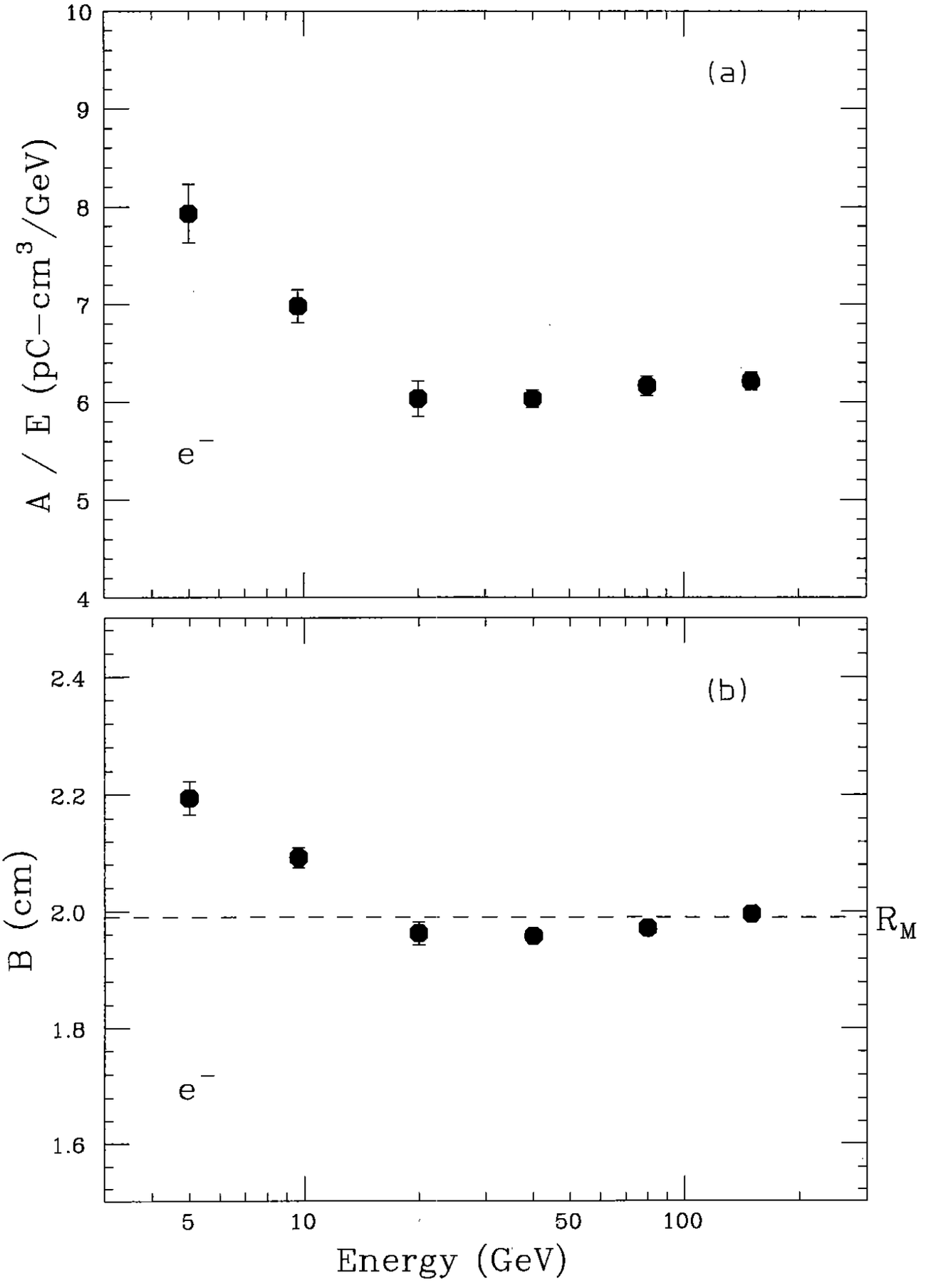
(a)
A / E (pC−cm^3/GeV)
10
9
8
7
6
5
4
e$^-$
(b)
B (cm)
2.4
2.2
2.0
1.8
1.6
R_M
e$^-$
5
10
50
100
Energy (GeV)

Fig. 7

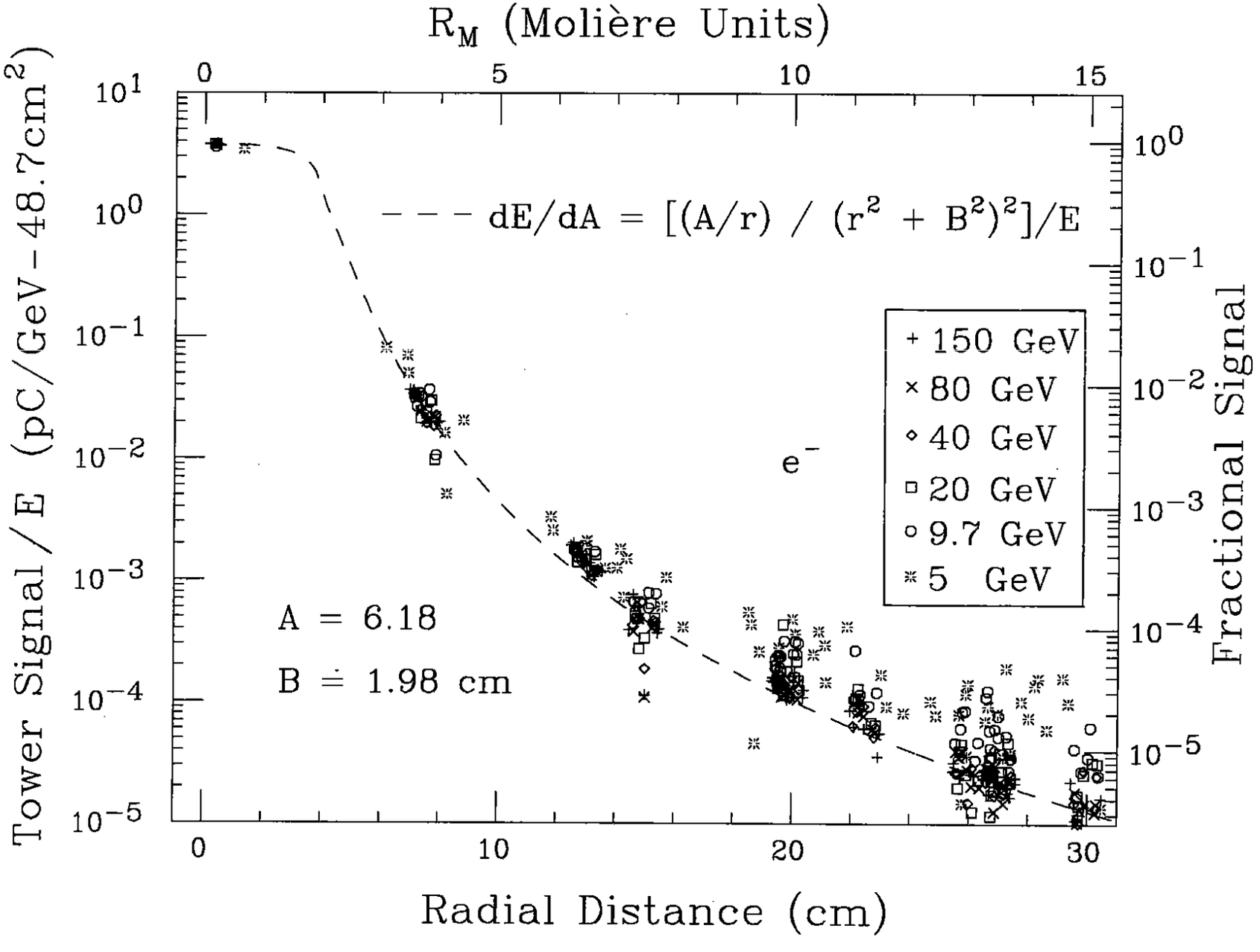
R_M (Molière Units)
0
5
10
15
10^1
10^0
10^{-1}
10^{-2}
10^{-3}
10^{-4}
10^{-5}
Tower Signal / E (pC/GeV-48.7cm^2)
10^0
10^{-1}
10^{-2}
10^{-3}
10^{-4}
10^{-5}
Fractional Signal
$--- dE/dA = [(A/r) / (r^2 + B^2)^2]/E$
e^-
+ 150 GeV
× 80 GeV
◇ 40 GeV
□ 20 GeV
○ 9.7 GeV
⁂ 5 GeV
A = 6.18
B = 1.98 cm
0
10
20
30
Radial Distance (cm)

Figure 8

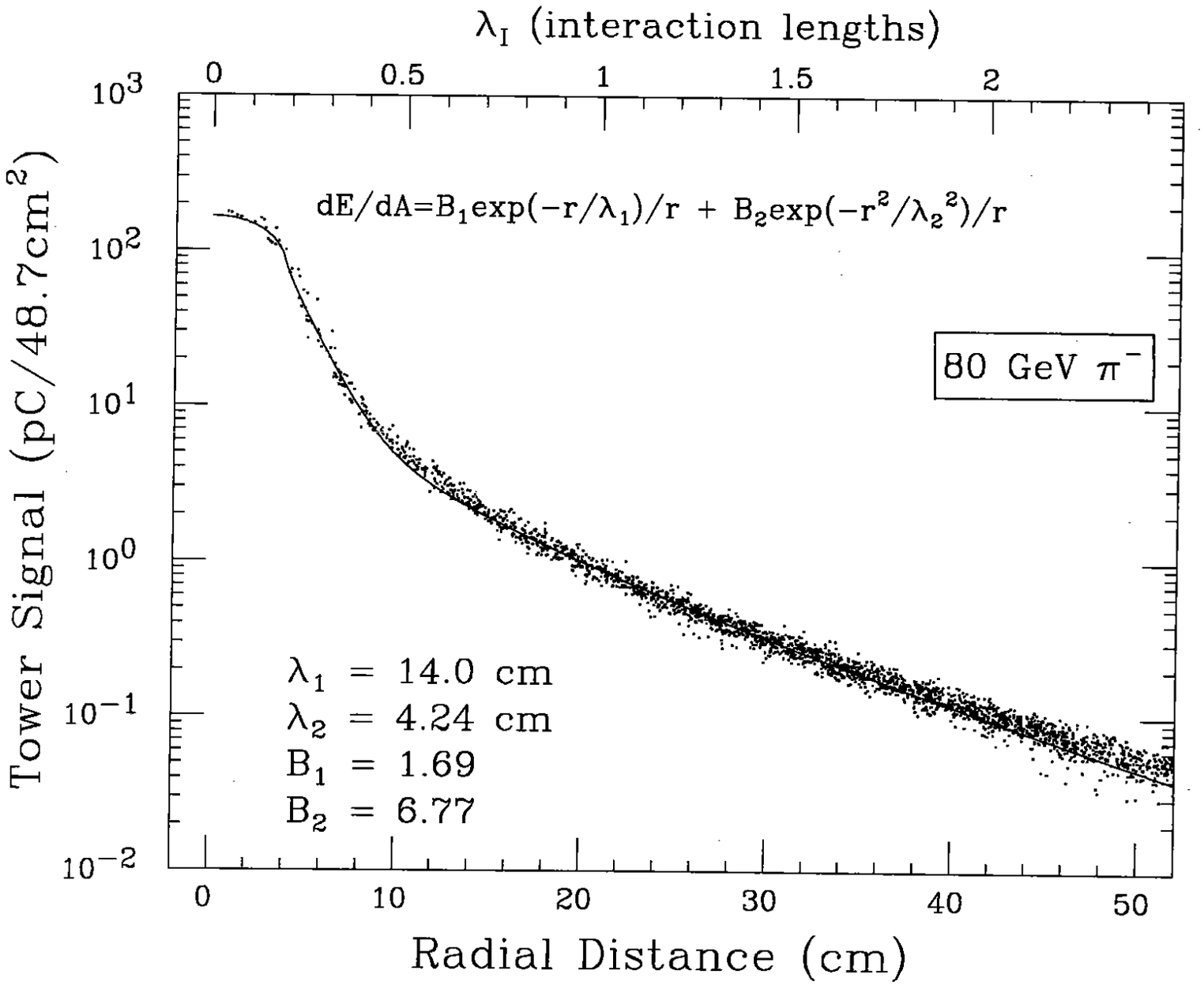
λI (interaction lengths)
0
0.5
1
1.5
2
10^3
10^2
10^1
10^0
10^-1
10^-2
Tower Signal (pC/48.7cm^2)
dE/dA=B1exp(−r/λ1)/r + B2exp(−r^2/λ2^2)/r
80 GeV π−
λ1 = 14.0 cm
λ2 = 4.24 cm
B1 = 1.69
B2 = 6.77
0
10
20
30
40
50
Radial Distance (cm)

Figure 9

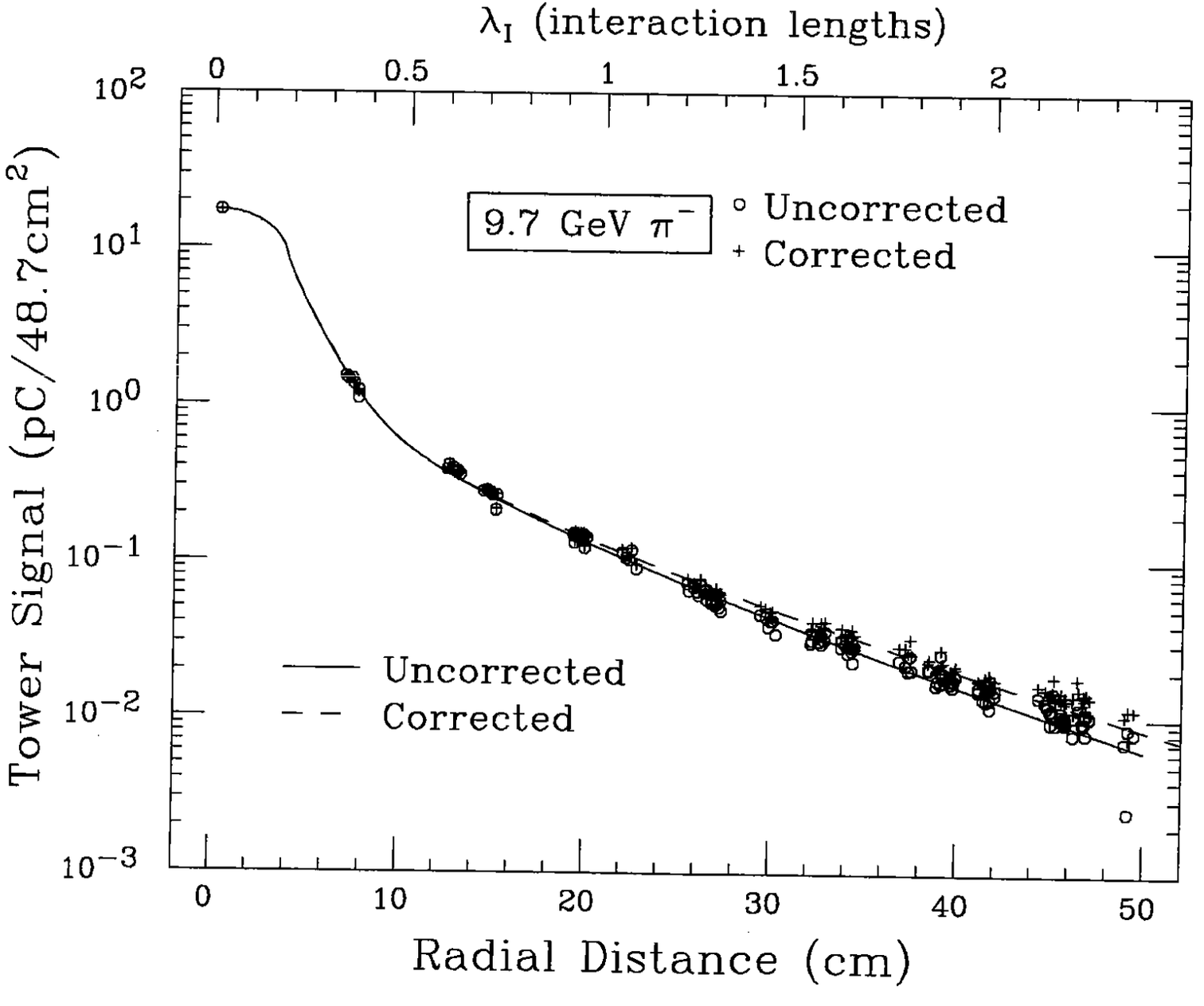
λ_I (interaction lengths)
0
0.5
1
1.5
2
10^2
10^1
10^0
10^{-1}
10^{-2}
10^{-3}
Tower Signal (pC/48.7cm^2)
9.7 GeV π^-
° Uncorrected
+ Corrected
Uncorrected
Corrected
0
10
20
30
40
50
Radial Distance (cm)

Figure 10

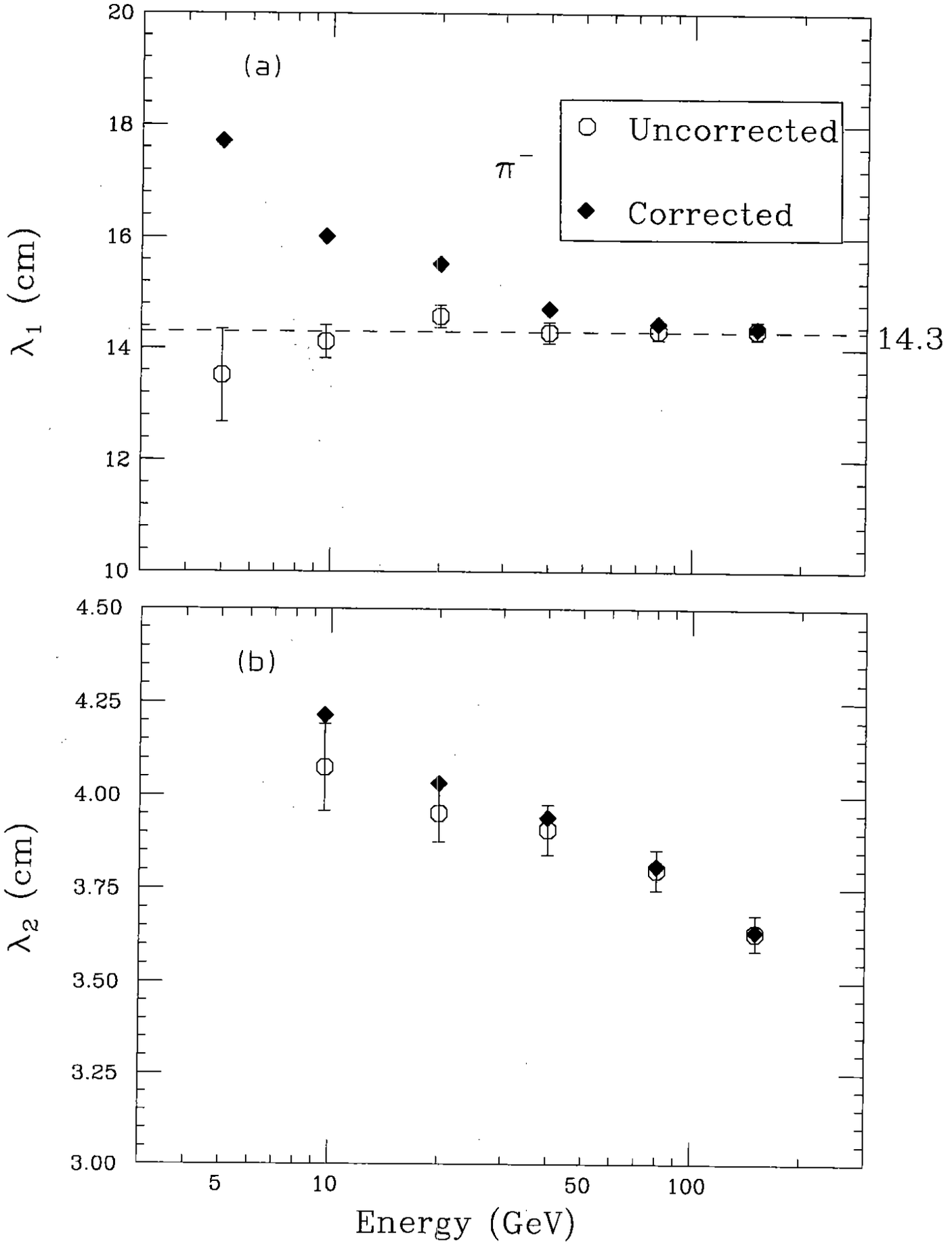
(a)
Uncorrected
Corrected
π^-
λ_1 (cm)
14.3
20
18
16
14
12
10
(b)
λ_2 (cm)
4.50
4.25
4.00
3.75
3.50
3.25
3.00
5
10
50
100
Energy (GeV)

Fig. 11

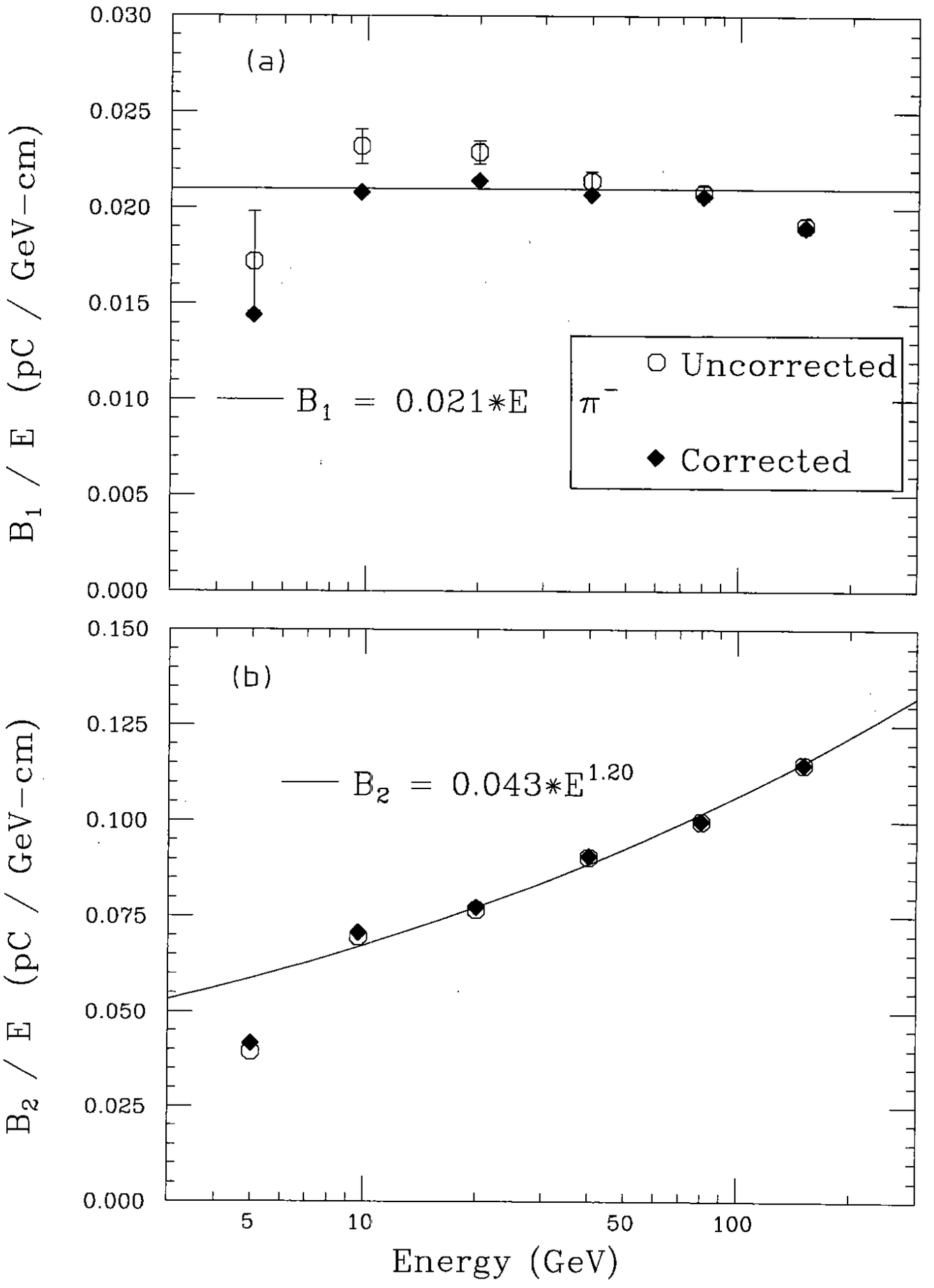
(a)
0.030
0.025
0.020
0.015
0.010
0.005
0.000
B_1 / E (pC / GeV−cm)
$B_1 = 0.021*E$
π^-
Uncorrected
Corrected
(b)
0.150
0.125
0.100
0.075
0.050
0.025
0.000
B_2 / E (pC / GeV−cm)
$B_2 = 0.043*E^{1.20}$
5
10
50
100
Energy (GeV)

Fig. 12

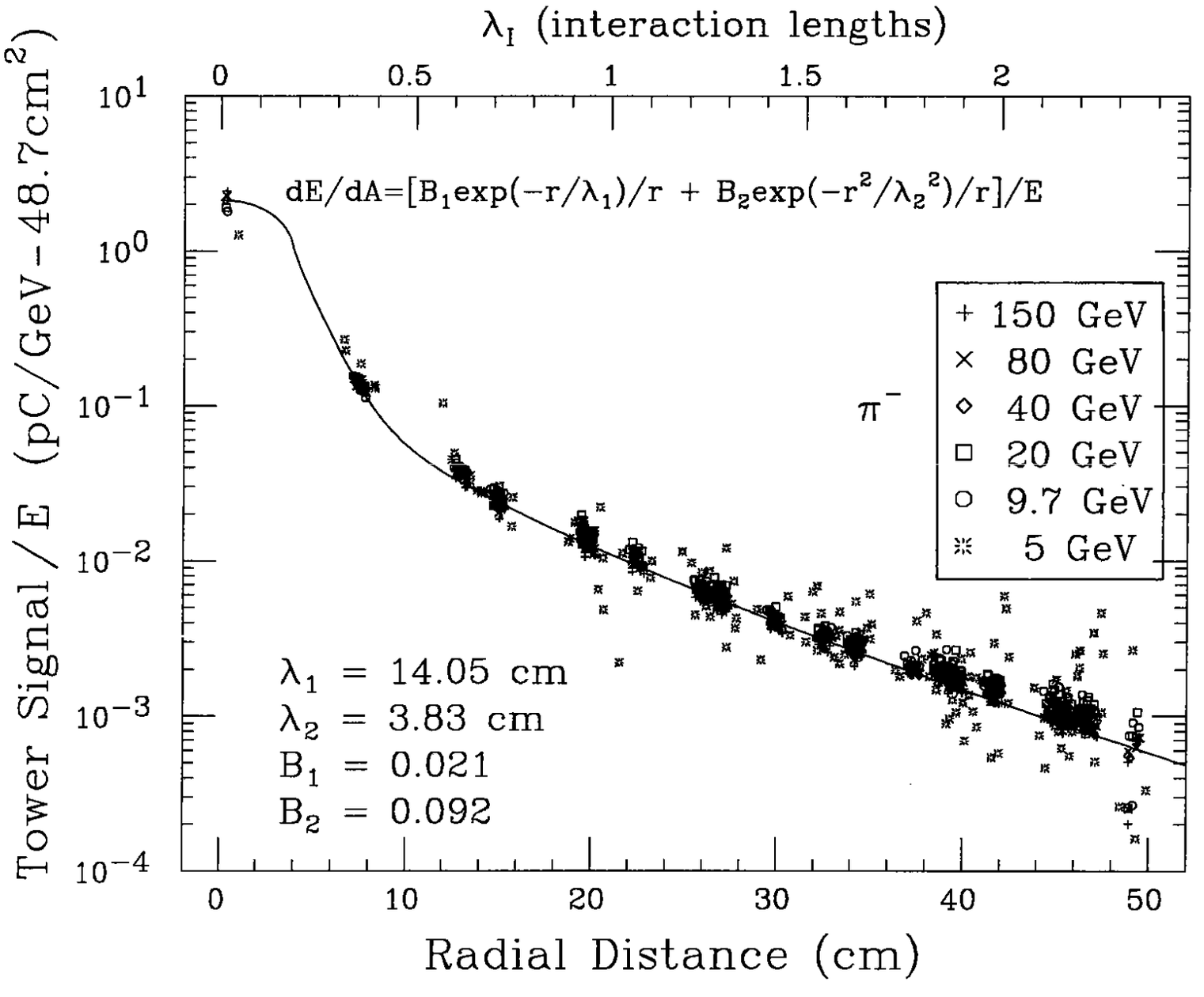
λ_I (interaction lengths)
0
0.5
1
1.5
2
10^1
10^0
10^{-1}
10^{-2}
10^{-3}
10^{-4}
Tower Signal / E (pC/GeV - 48.7cm^2)
$dE/dA=[B_1\exp(-r/\lambda_1)/r + B_2\exp(-r^2/\lambda_2^2)/r]/E$
+ 150 GeV
× 80 GeV
◇ 40 GeV
□ 20 GeV
○ 9.7 GeV
※ 5 GeV
π^-
λ_1 = 14.05 cm
λ_2 = 3.83 cm
B_1 = 0.021
B_2 = 0.092
0
10
20
30
40
50
Radial Distance (cm)

Figure 13

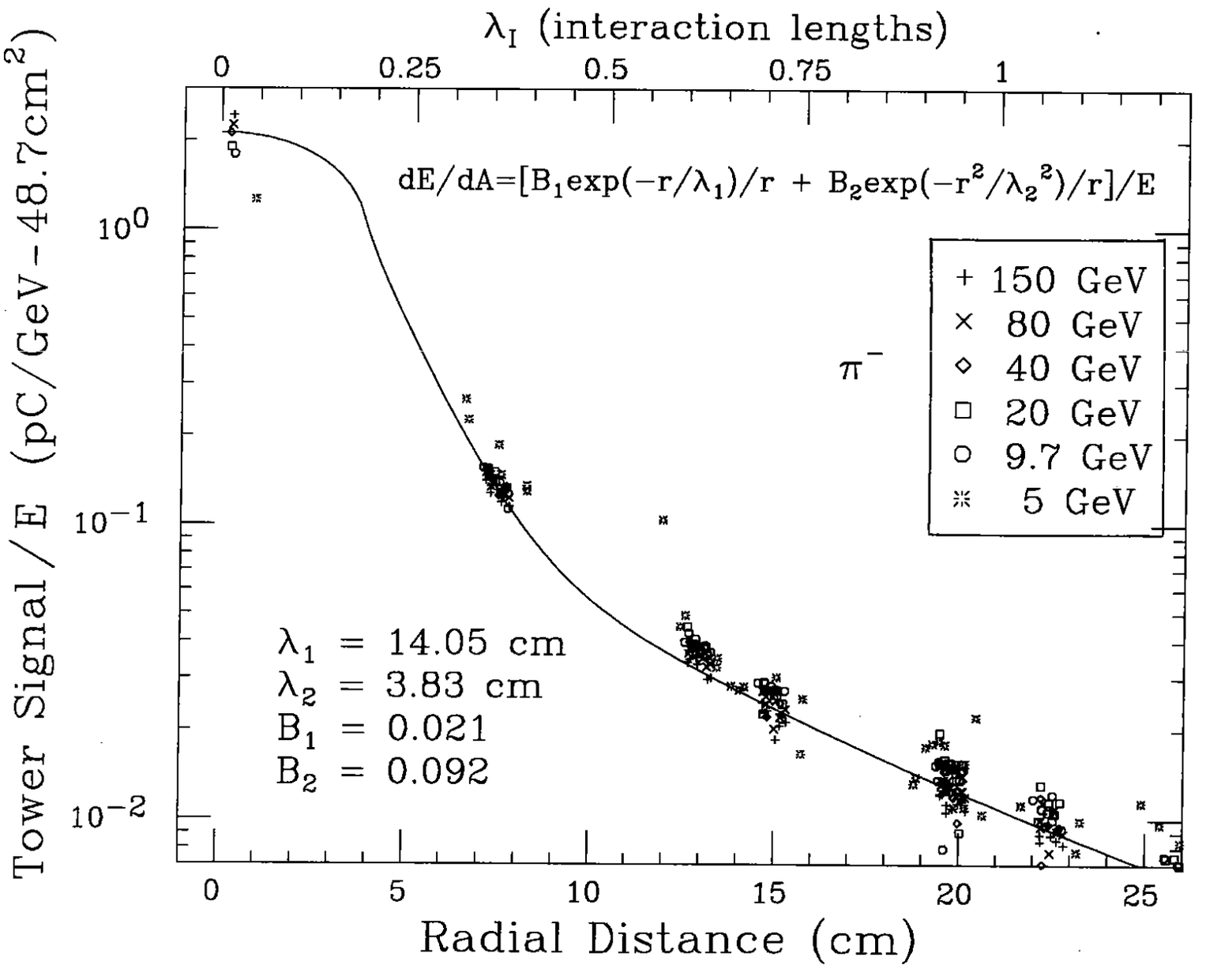
λ_I (interaction lengths)
0
0.25
0.5
0.75
1
$dE/dA=[B_1\exp(-r/\lambda_1)/r + B_2\exp(-r^2/\lambda_2^2)/r]/E$
π^-
+ 150 GeV
× 80 GeV
◇ 40 GeV
□ 20 GeV
○ 9.7 GeV
⁂ 5 GeV
λ_1 = 14.05 cm
λ_2 = 3.83 cm
B_1 = 0.021
B_2 = 0.092
Tower Signal / E (pC/GeV-48.7cm^2)
10^0
10^{-1}
10^{-2}
0
5
10
15
20
25
Radial Distance (cm)

Figure 14

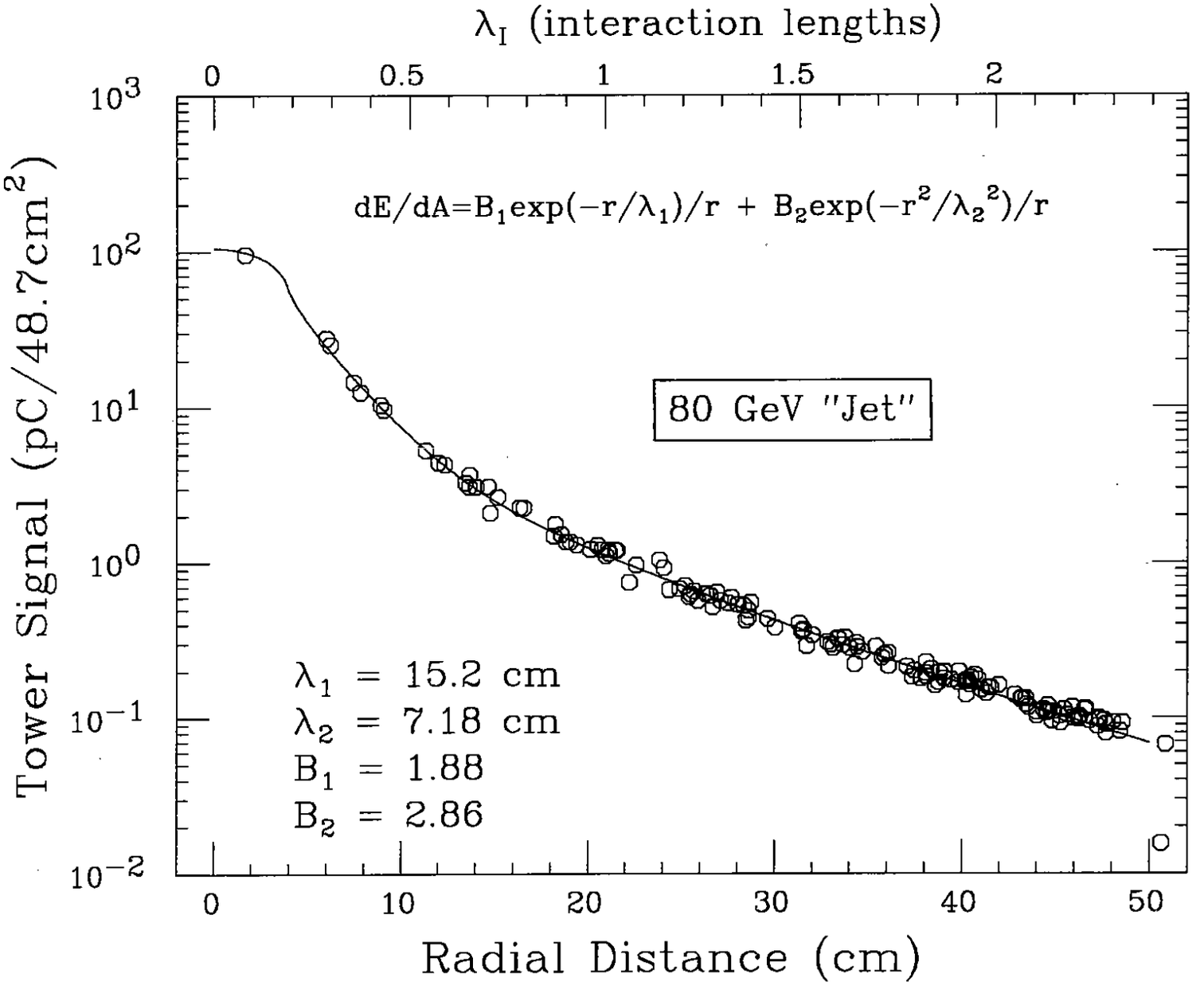
λ_I (interaction lengths)
0
0.5
1
1.5
2
10^3
10^2
10^1
10^0
10^{-1}
10^{-2}
Tower Signal (pC/48.7cm^2)
$dE/dA=B_1\exp(-r/\lambda_1)/r + B_2\exp(-r^2/\lambda_2{}^2)/r$
80 GeV "Jet"
λ_1 = 15.2 cm
λ_2 = 7.18 cm
B_1 = 1.88
B_2 = 2.86
0
10
20
30
40
50
Radial Distance (cm)

Figure 15

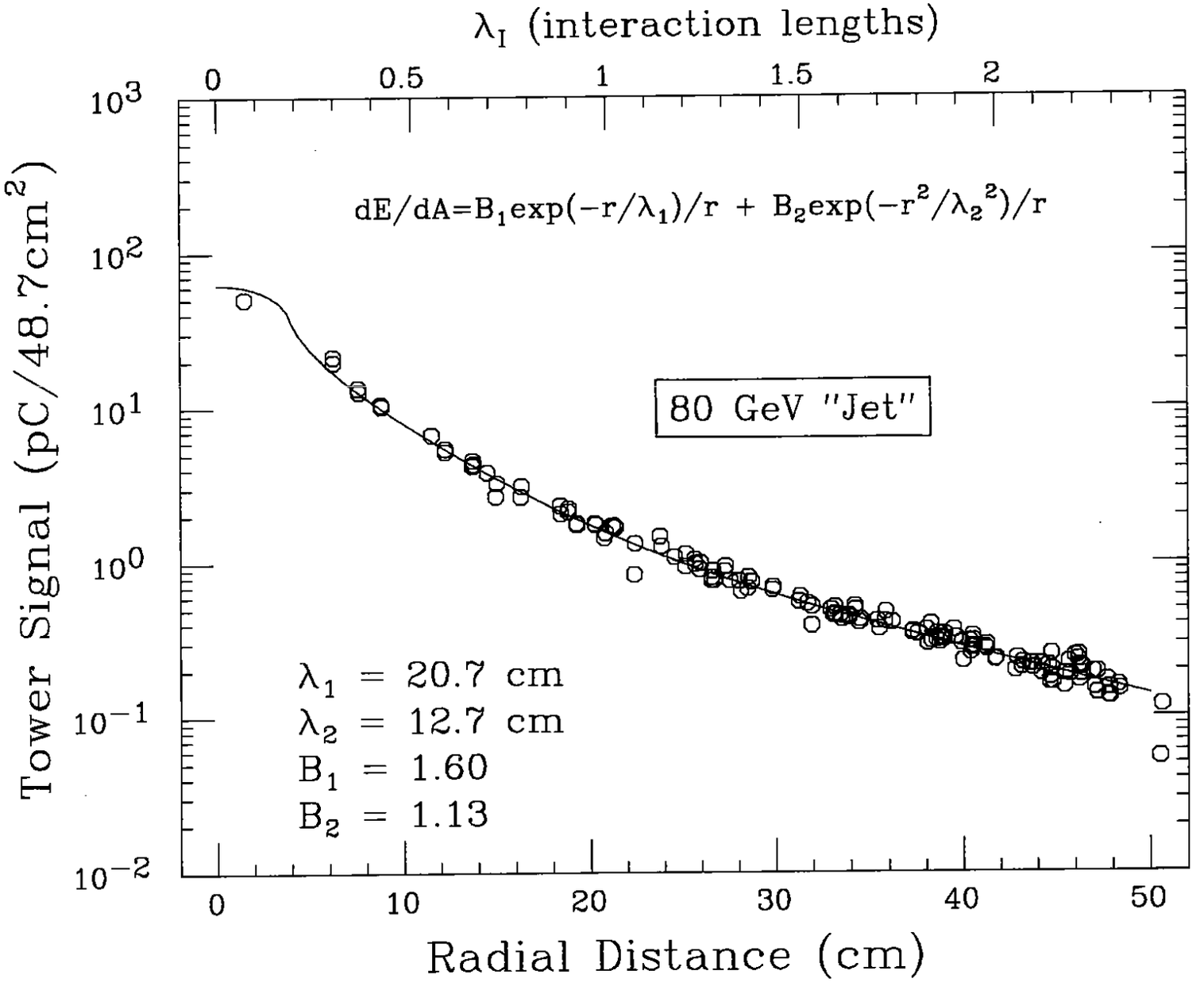
λ_I (interaction lengths)
0
0.5
1
1.5
2
10^3
10^2
10^1
10^0
10^{-1}
10^{-2}
Tower Signal (pC/48.7cm^2)
dE/dA=B_1exp(−r/λ_1)/r + B_2exp(−r^2/$\lambda_2{}^2$)/r
80 GeV "Jet"
λ_1 = 20.7 cm
λ_2 = 12.7 cm
B_1 = 1.60
B_2 = 1.13
0
10
20
30
40
50
Radial Distance (cm)

Figure 16

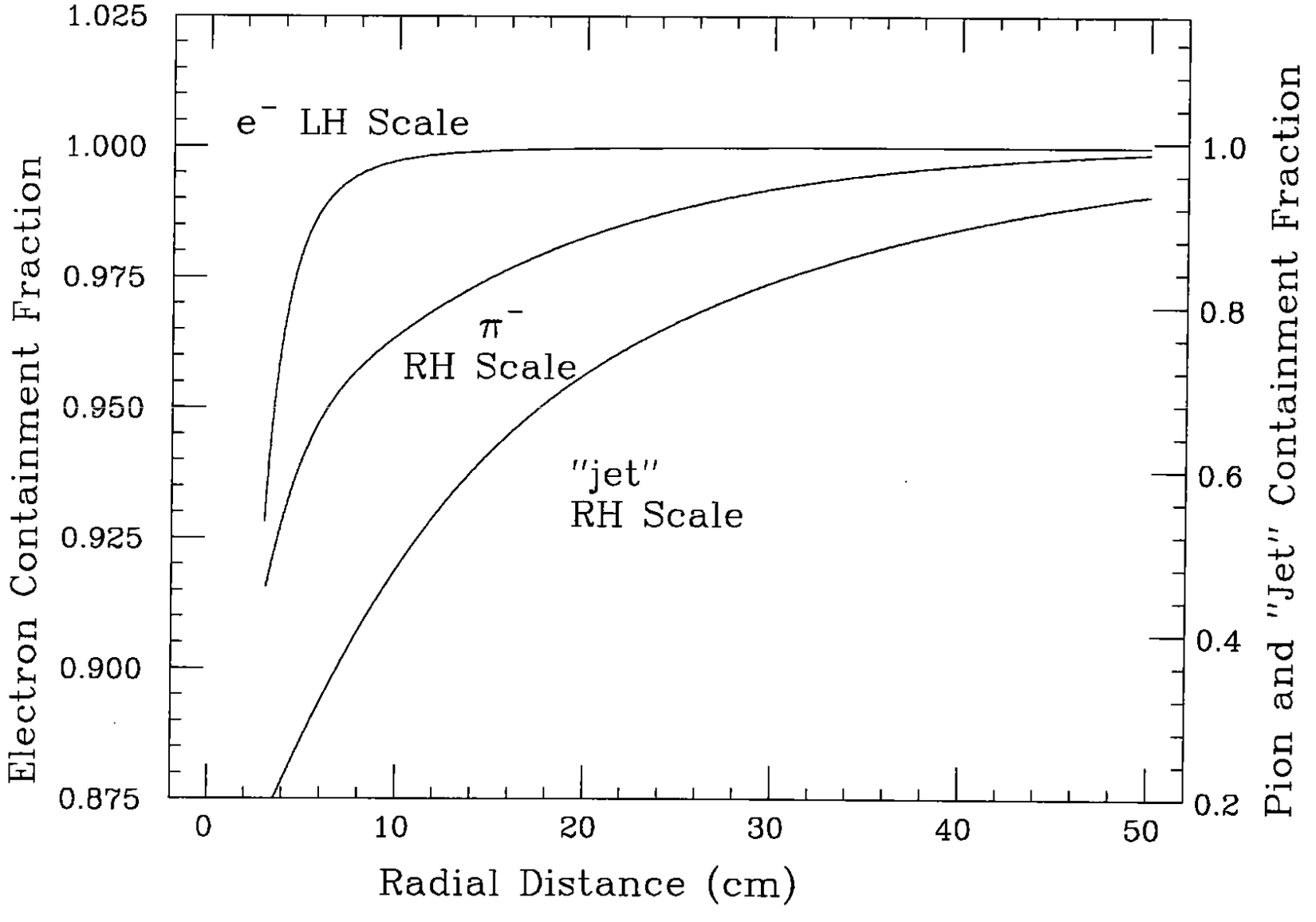
1.025
1.000
0.975
0.950
0.925
0.900
0.875
Electron Containment Fraction
e⁻ LH Scale
π⁻
RH Scale
"jet"
RH Scale
0
10
20
30
40
50
Radial Distance (cm)
1.0
0.8
0.6
0.4
0.2
Pion and "Jet" Containment Fraction

Figure 17

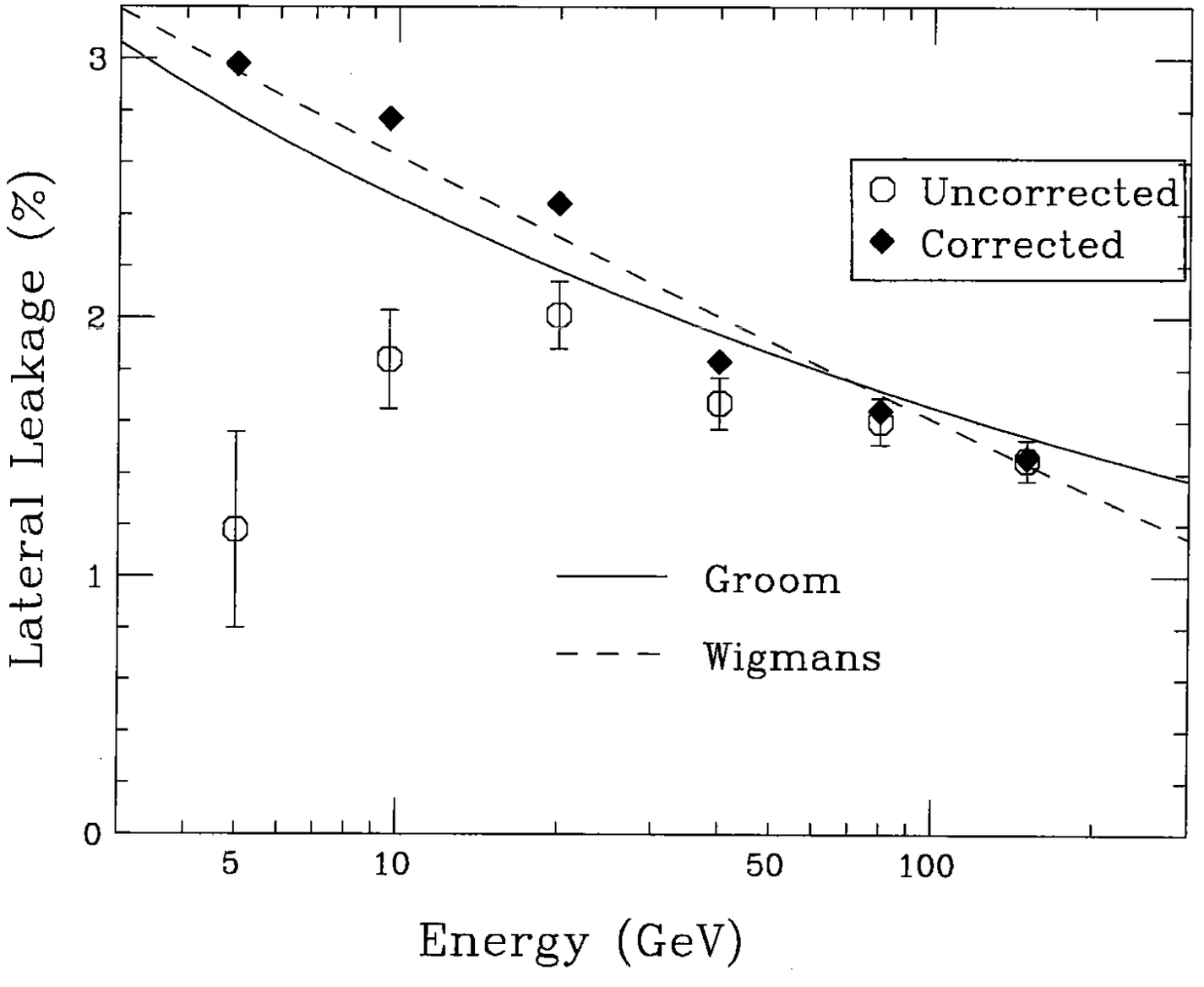
Lateral Leakage (%)
3
2
1
0
5
10
50
100
Energy (GeV)
Uncorrected
Corrected
Groom
Wigmans

Figure 18

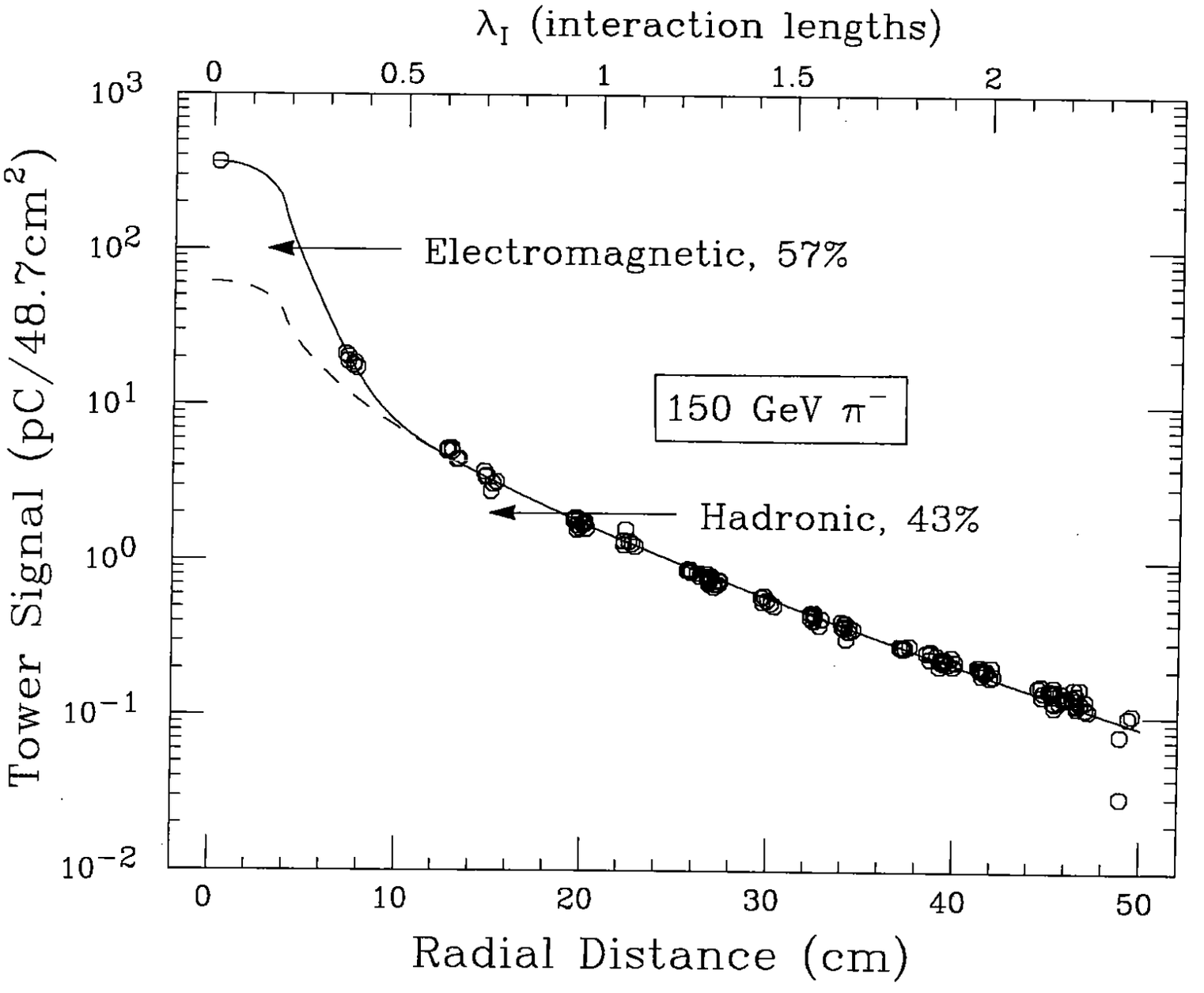
λ_I (interaction lengths)
0
0.5
1
1.5
2
10^3
10^2
10^1
10^0
10^{-1}
10^{-2}
Tower Signal (pC/48.7cm^2)
Electromagnetic, 57%
150 GeV π^-
Hadronic, 43%
0
10
20
30
40
50
Radial Distance (cm)

Figure 19

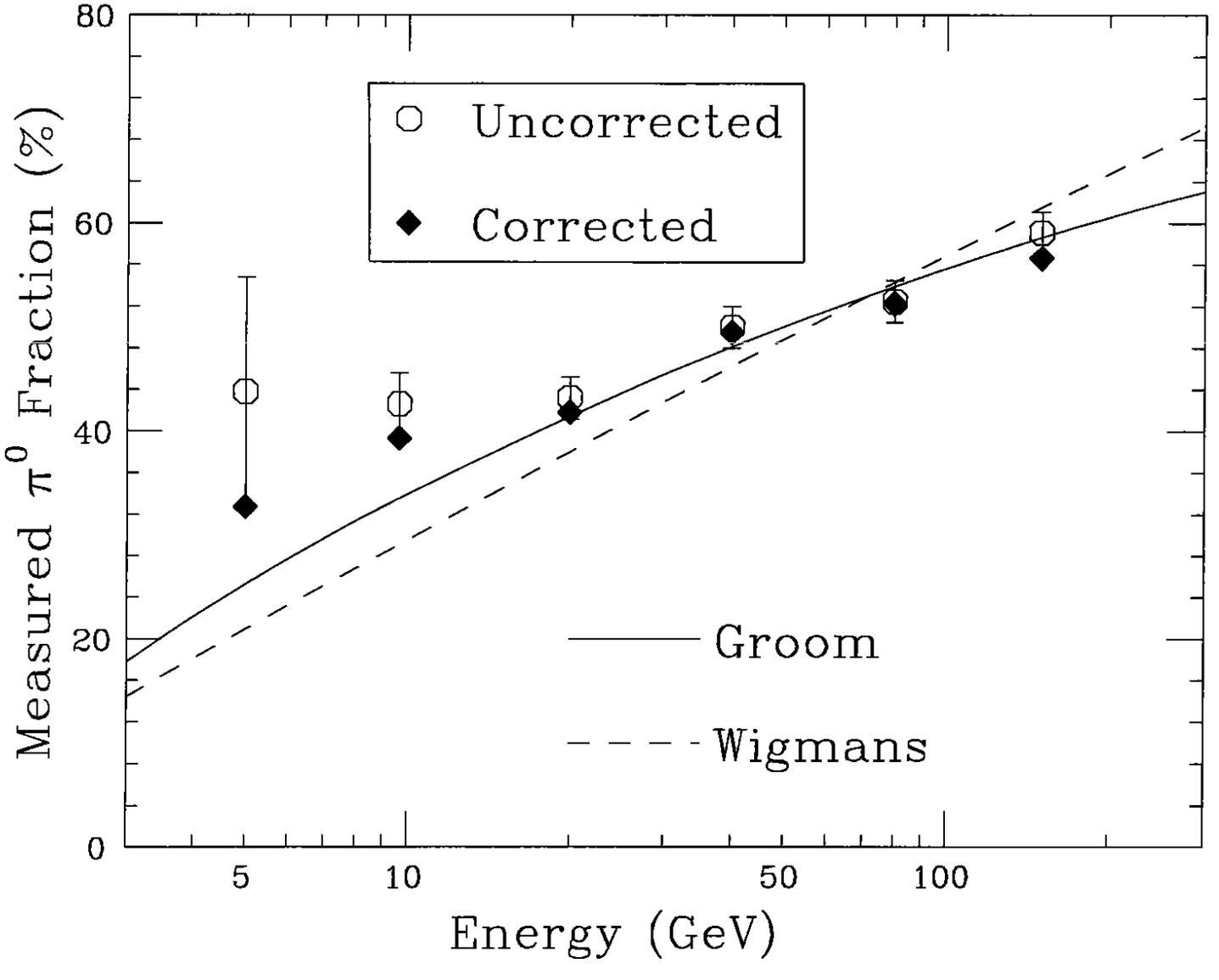
Uncorrected
Corrected
Groom
Wigmans
Measured π^0 Fraction (%)
Energy (GeV)
0
20
40
60
80
5
10
50
100

Figure **20**

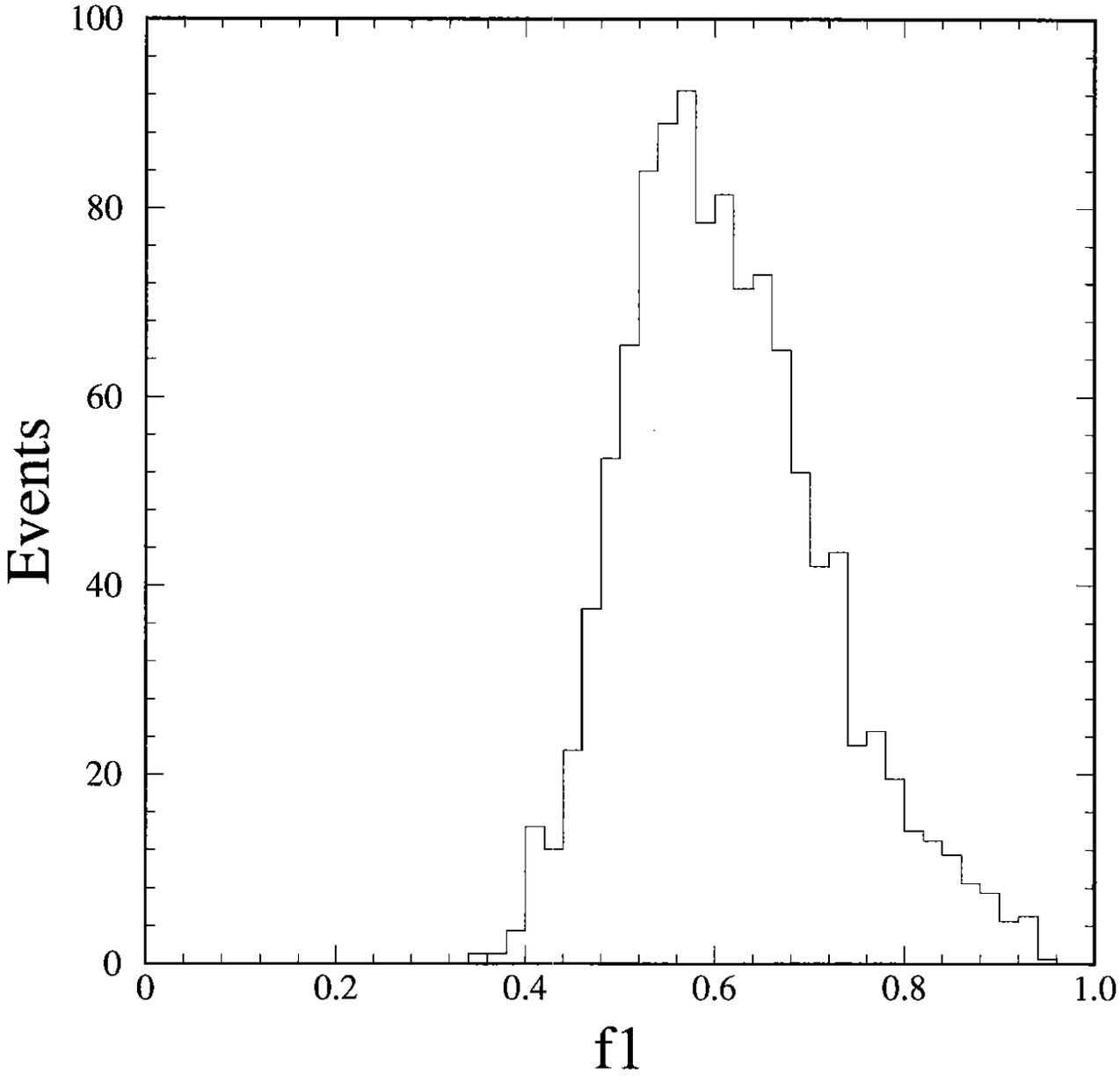

Figure 21

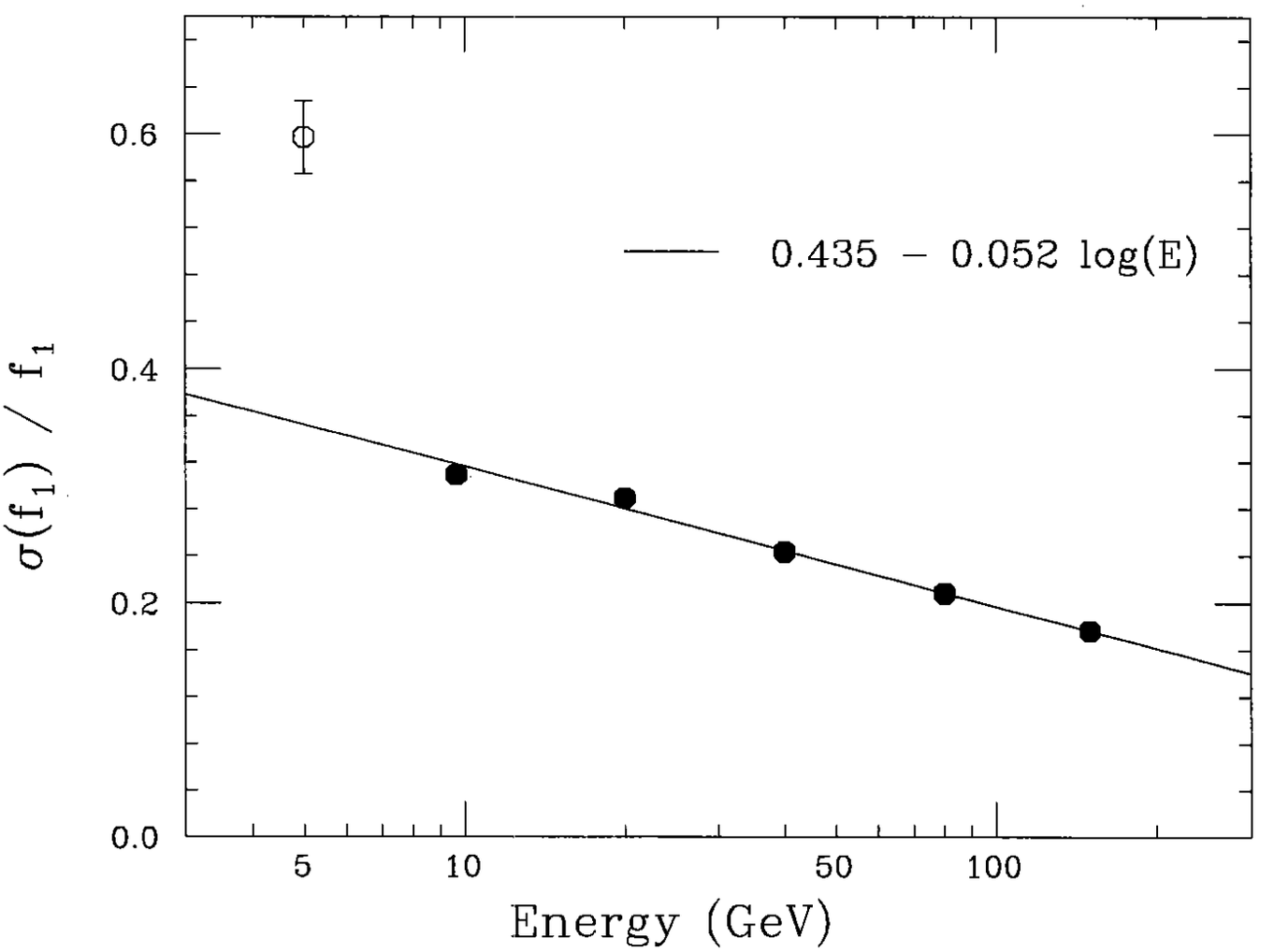

Figure 22

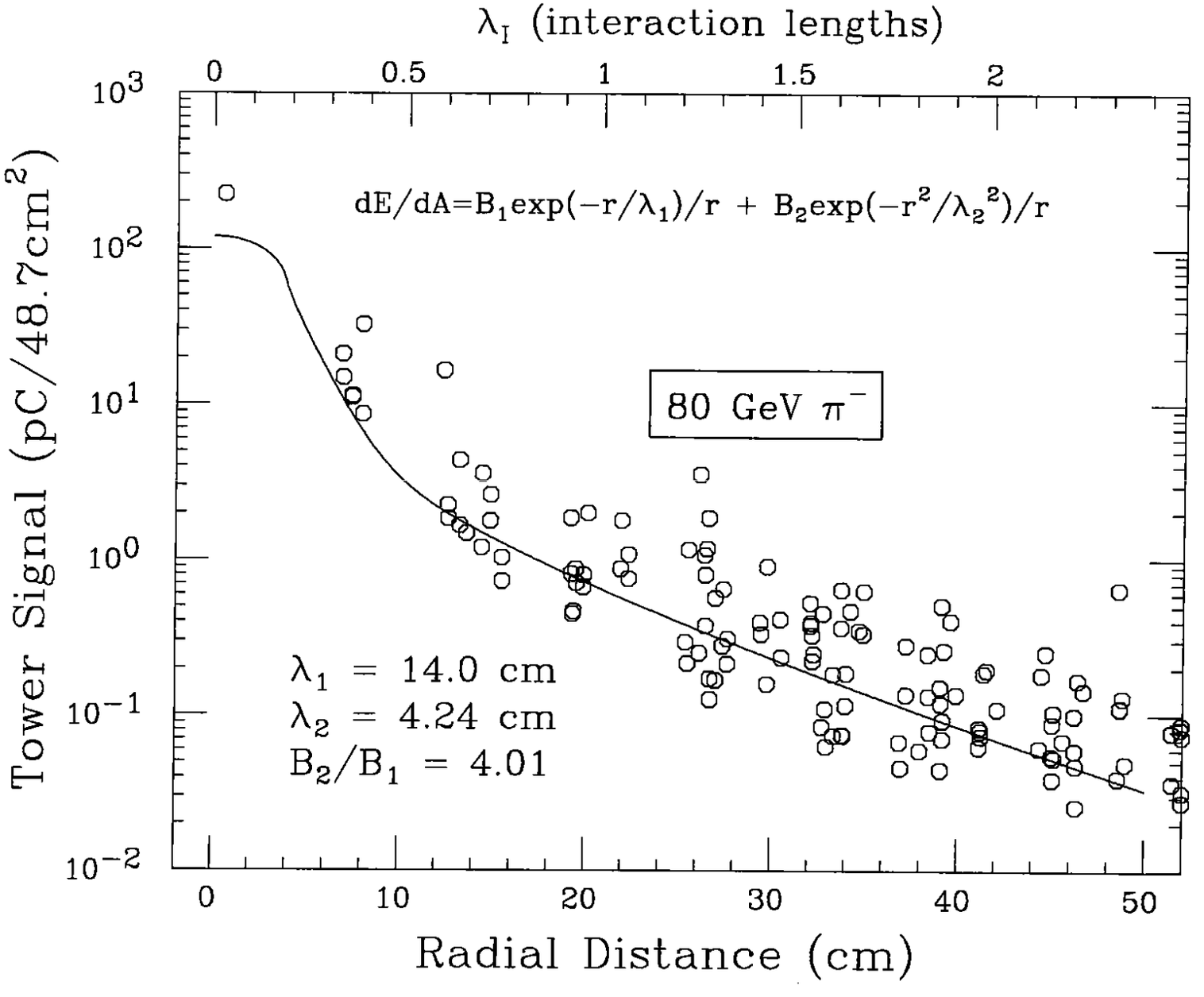
λI (interaction lengths)
0
0.5
1
1.5
2
dE/dA=B1exp(−r/λ1)/r + B2exp(−r²/λ2²)/r
80 GeV π⁻
λ1 = 14.0 cm
λ2 = 4.24 cm
B2/B1 = 4.01
Tower Signal (pC/48.7cm²)
Radial Distance (cm)

Figure **23**

Imprimé au CERN. Prix: 1.60 Fr.

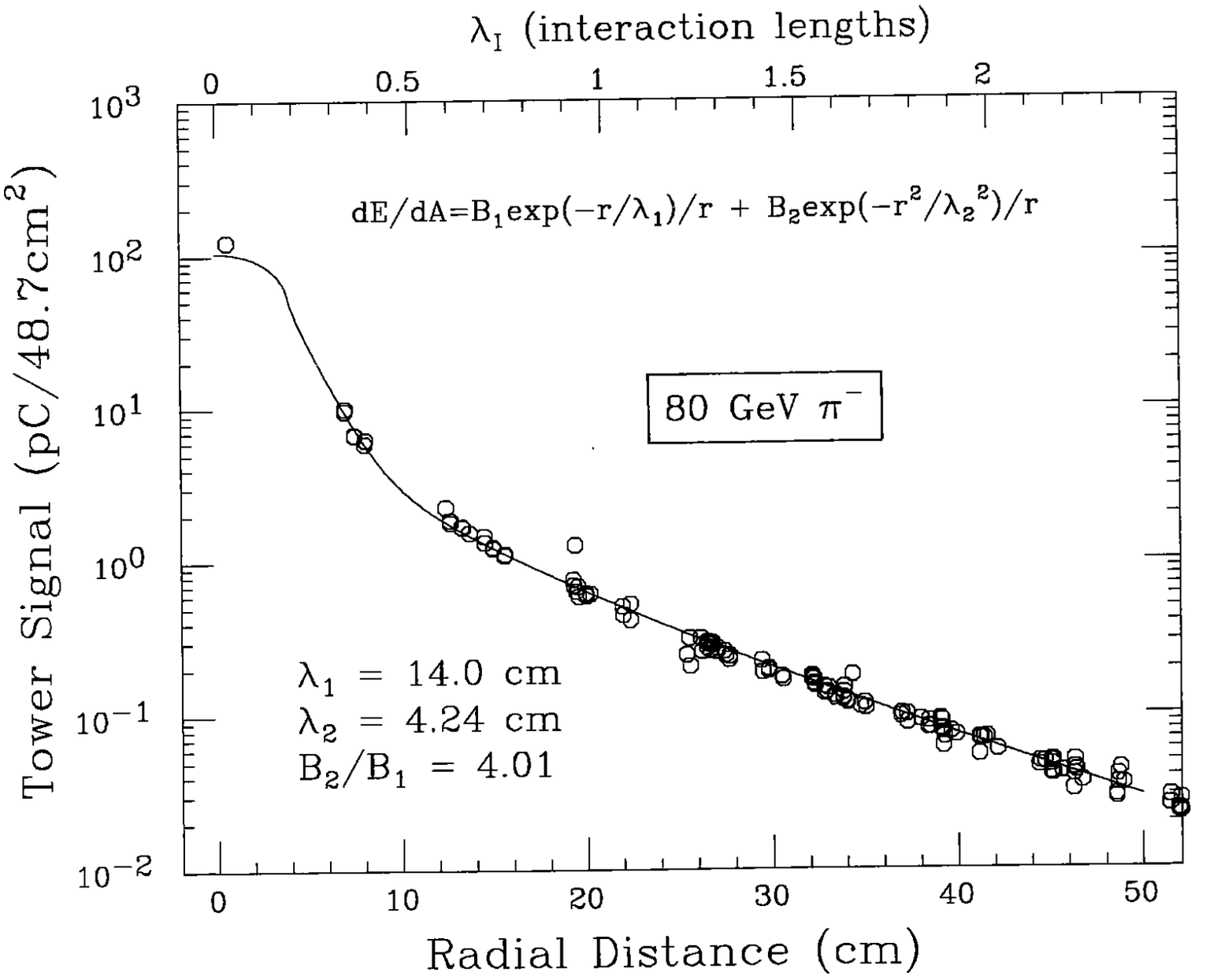

Figure 24